

Chapter 5

Graphene electrodes

Since graphene was discovered in 2004³², the research has witnessed many advances in the mass production of this material and in the determination of its feasible applications. In fact graphene features exceptional structural and electronic properties combining extraordinary mechanical strength, exceptionally high electronic and thermal conductivities, impermeability to gases, as well as many other characteristics, all of which make it highly attractive for a wide number of applications.

In graphene, carbon atoms form a hexagonal lattice on a two-dimensional plane with $C - C$ bond lengths of about 1.42 Å. Each carbon forms three σ bonds with its three neighbors, and share the remaining π electron giving rise to two π electron clouds above and below the lattice plane. In the electronic structure, this gives rise to a π and π^* bands, responsible for most of the peculiar electronic properties of graphene. Specifically these bands meet at two non-equivalent points labeled K and K' , usually called Dirac points, causing graphene to be a zero-gap semiconductor, as shown in fig. 5.1.

Thus K and K' points are of primary interest to understand the electronic properties of graphene as opposite of traditional semiconductors where the main point of interest in the bandstructure is generally Γ , where momentum is zero.

One of main characteristic of graphene bands is the linear dispersion relation in proximity of the Dirac points. This linear dispersion around K points is well-described by the Dirac equation for massless fermions:

$$E_{\pm}(k) \approx \pm \hbar v_f |k - K| \quad (5.1)$$

which corresponds to the spectrum of the Dirac-like Hamiltonian for low-energy massless Dirac fermions, *i. e.*, the effective mass of the charge carriers in this region is

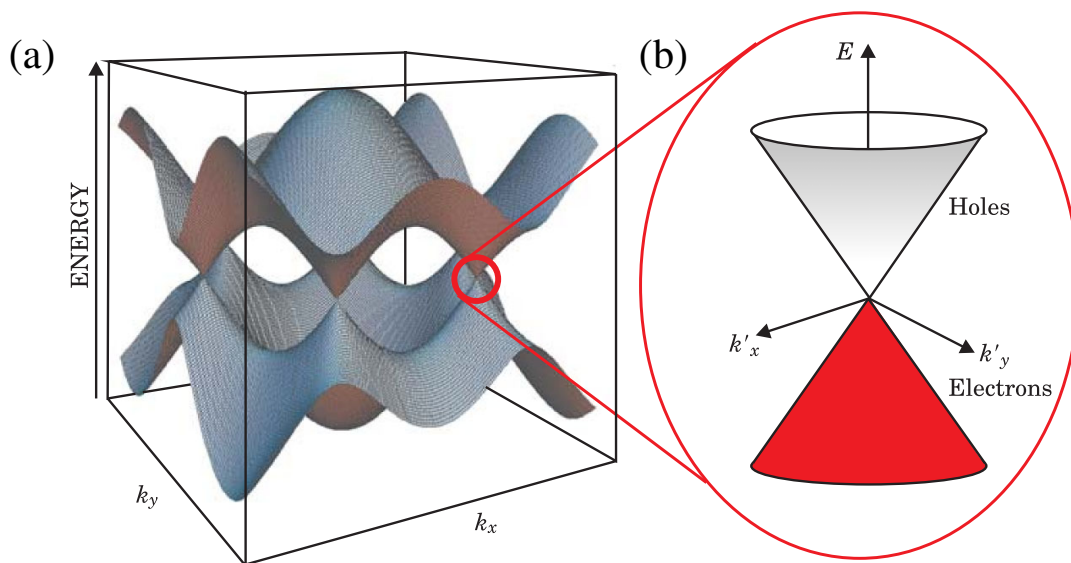


FIGURE 5.1: (a) Graphene band-structure. (b) Enlargement of the bandstructure close to the Dirac points. From ref. [Sarma et al.¹²²].

zero. Since $v_f \sim 10^6$ m/s ($\sim 1/300$ -th the speed of light in vacuum) charge carriers in graphene behave like relativistic particles traveling with an effective speed of light given by the Fermi velocity.

Thanks to its unique band structure, graphene exhibits transport properties such as minimum conductivity, ambipolar field effect and Klein tunneling, which are absent in most conventional materials¹²³. This unusual electronic behavior leads to exceptional transport properties in comparison to common semiconductors.

In ideal graphene (or at most with few impurities or defects) the transport is ballistic over large distances, since carriers can travel at the Fermi velocity (v_f) from one electrode to the other without scattering. In this case the Fermi energy is at the Dirac point, where the material has vanishing density of states. Despite this a minimum value for the conductivity ($4e^2/\pi h$) has been theoretically predicted and experimentally measured.

Otherwise, ambipolar field effect arise from the fact the Fermi level can be easily moved into the conduction or valence bands by applying an external electric field or simply depositing it on a electron withdrawing or donor substrate, allowing conduction by either holes or electrons.

Another peculiar property of graphene is that charge carriers cannot be confined by electrostatic potentials. In traditional semiconductors, if an electron strikes an electrostatic barrier higher than the electron energy, the electron wavefunction will exponentially decay within the barrier. As opposite, if the particle obeys the Dirac equation, its transmission probability increases with increasing the barrier height. Indeed a Dirac

electron that hits a tall barrier will turn into a hole and propagate through the barrier until it reaches the other side, where it will turn back into an electron. This phenomenon is known as Klein tunneling.

Although graphene can transport electrons extremely quickly, which could allow the realization of very fast switching speed electronic elements – graphene-based transistors could run at speeds a hundred to a thousand times faster than traditional silicon transistors – it also shows a significant drawback if compared with the conventional silicon devices. Indeed, even though graphene can be switched between states with different electrical conductivity, which is the main characteristic of semiconductor devices, the on/off ratio is not very high. That means that graphene continues to conduct even in its “off” state and this is significant drawback if one wants to replace Si-based technologies where on/off ratios of $\sim 10^7$ are commonly achieved. Such a ratio could be achieved in graphene only by opening a bandgap at the Dirac point in order to suppress the band-to-band tunneling. It has been predicted that a bandgap of 0.4 eV could achieve the desired effect³³.

Many solutions have been proposed to engineer this bandgap. One possibility is the use of bilayer graphene, allowing to open a bandgap by breaking the symmetry of the bilayer stack with the application of a transverse electrical field¹²⁴. A second technique is based on the confinement of the charge carriers in a nanoribbon, effectively obtaining a “1D” structure¹²⁵. Another approach involves the patterned hydrogen adsorption. In particular graphene deposited on Ir give rise to a Moiré pattern, that remains also after hydrogen adsorption¹²⁶. For such system, theoretical DFT simulations predict a gap of ~ 0.43 eV, close to desired value of 0.4 eV.

Here we consider a different graphene-based structure, suitable for applications in molecular devices, constituted by a freestanding carbon chain contacted with graphene leads, as those shown in fig. 5.2. These structures can be prepared experimentally with a top-down approach involving the sputtering of carbon atoms from a graphene ribbon by means of an highly energetic TEM electron beam. In practice the basic idea is to thin a graphene nanoribbon from its open ends by removing the excess of carbon atoms row by row while a single chain is obtained. This method has been addressed at length in chapter 2.

Specifically the investigation presented in this chapter somehow parallel the study carried out for Ag-chain-Ag systems present in chapter 4, with the aim to determine the issues relevant for the transport properties in graphene-chain-graphene structures.

To this aim we first considered single chains connected to zigzag nanoribbons, investigating their geometrical and electronic structure in order to establish a connection with

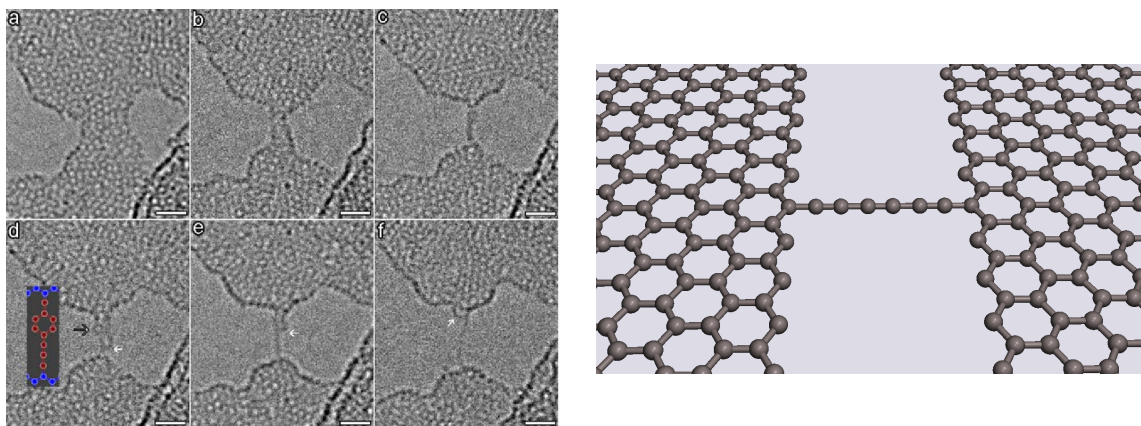


FIGURE 5.2: Left: High resolution TEM images showing the dynamics for the formation of a freestanding carbon chain⁶⁹. Right: Structure investigated throughout this chapter.

their transport properties. In particular, we focused on the role of the contact geometry. First we considered chains contacted either in correspondence of the outermost or the innermost atom of the edge of an ideal zigzag edge-shaped nanoribbon, finding that the latter lead to an overall reduction of the transmission probabilities. Next we investigated chains connected to the ribbon through tips of different size and shape, which turns out to have dramatic effects on the transport properties.

We also studied the transport characteristics of double chains at different interchain distances, observing qualitative different interference patterns depending on the chain length, the interchain distance and the contact geometry. We also address the possibility to achieve chemical gating in such structures, induced by a lithium atom placed alongside a chain.

We further examined the possibility to switch the current on and off by mechanical rotation of a benzenic or a polycyclic aromatic group inserted in the middle of the chain, finding that such system show the potential for applications as molecular switches.

Finally we briefly investigated the transport properties of single chains contacted with armchair ribbons, pointing out on the role of different junction configurations in determining the transmission probabilities.

5.1 Computational setup

The electronic structure calculations have been carried out at density functional theory (DFT) level as implemented in the SIESTA code⁹⁵ using the Perdew-Burke-Ernzerhof

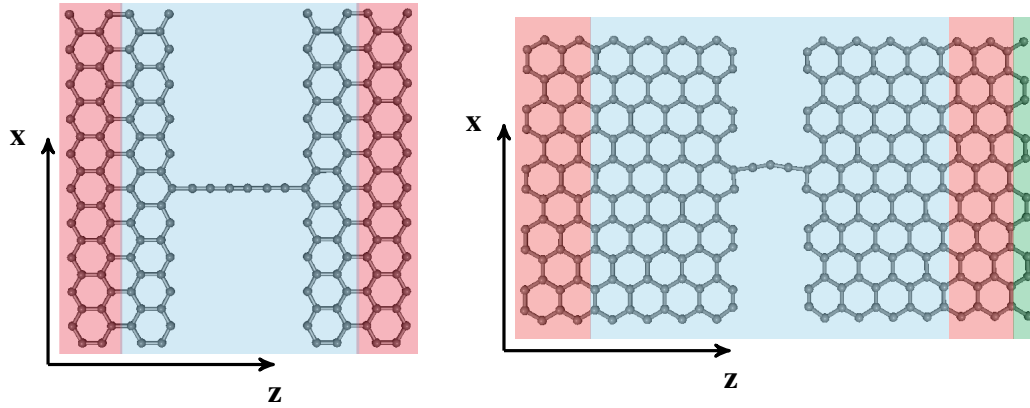


FIGURE 5.3: Setup of zigzag and armchair devices. Red: electrodes; light blue: scattering region, green: buffer layers. z is the transport direction, y the direction orthogonal to the electrode plane.

(PBE) functional to describe the exchange-correlation effects.

Core electrons are replaced by Troullier-Martins norm-conserving pseudopotential¹⁰⁰ and the valence electrons are expanded in a localized single- ζ *plus* polarization (SZP) basis set. Cut-off radii of atomic orbitals has been determined by setting the confinement energy to 0.02 Ry and an energy cutoff of 300 Ry has been used for the real-space integration of the electron density.

The simulation cells considered in our calculations for the zigzag and armchair configurations are shown in fig. 5.3, along with their separation in electrodic and scattering regions. A buffer layer has been added to the armchair cell, in order to achieve proper boundary conditions, and $\sim 12 \text{ \AA}$ of vacuum are introduced above the graphene sheet in order to avoid interactions with the repeated images. The relative positions of the atoms included in the electrodic regions has been kept fixed during the optimization steps, while a threshold of 0.01 eV/\AA on the absolute value of the force acting on the other atoms has been adopted. Lattice vectors has also been relaxed.

The k -space sampling has been performed adopting the Monkhorst-Pack scheme and using a 3×1 k -mesh for the self-consistent steps in the optimization calculations that has been increased to 20×1 in the transport calculations and to 100×1 for the computation of the transmission probabilities.

The electron transport calculations has been performed using non-equilibrium Green's function method combined with DFT Hamiltonian as implemented in the TranSIESTA simulation package⁹⁶, within the formalism described in chapter 3.

5.2 Zigzag electrodes

5.2.1 Single chains

In this section we focus on single chains connected to zigzag edge-shaped electrodes either in correspondence of the outermost or the innermost atom of the edge, thus forming a single bond (C_n) or a four-atom ring ($C_n R$) at the junction, respectively (see fig. 5.4). These geometries show rather different geometrical and electronic structure depending on the number of carbon atoms. In particular, we analyzed a number of issues in order to determine how the structure influences the electronic properties and, in turn, the transport properties.

First, we determined the bond lengths of C_{11} and C_{12} chains, as reported in fig. 5.5. It is evident that C_{11} features a nearly cumulenic behavior in both configurations, with a

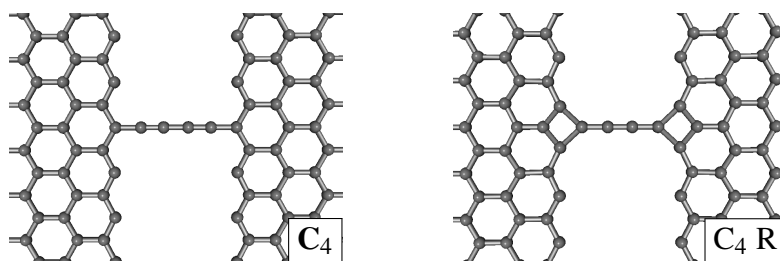


FIGURE 5.4: Structures of C_4 and $C_4 R$

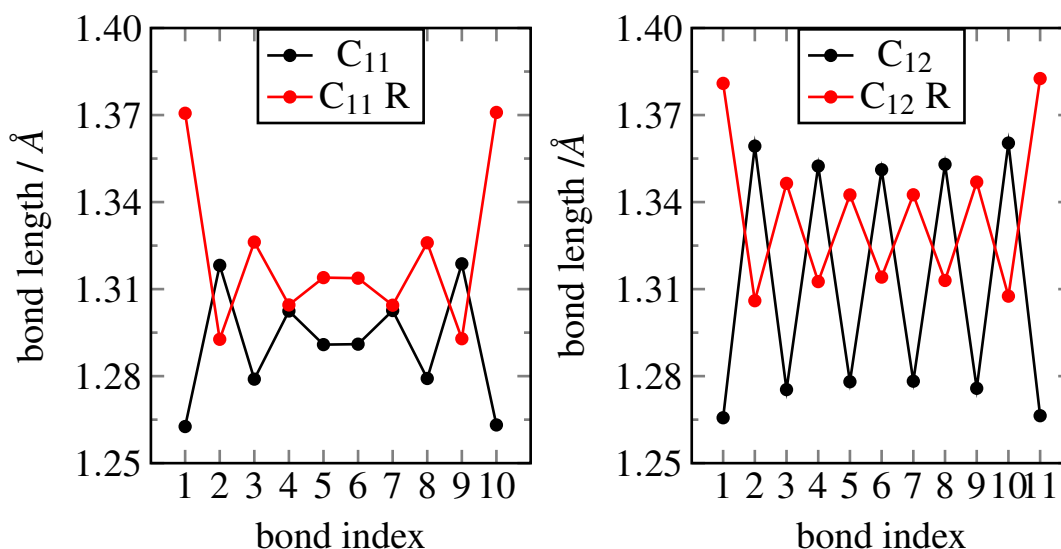
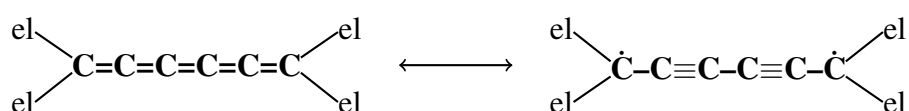


FIGURE 5.5: Bond lengths of C_{11} , C_{12} and corresponding R chains.

bond length alternation* (BLA) that increases from the middle to the end of the chain as a consequence of the binding of the electrodes. Even chains turn out to be polyynic in both cases, but C_{12} R shows a more cumulenic character, with BLA values in average about 2.5 times lower than C_{12} . It is obvious that the junction configuration is the main responsible for this different behavior, the C_{12} R chain being forced to be more cumulenic as a consequence of the ring geometry. Even more evident is the inversion of the BLA for both R chains, which feature short bonds where C_n chains have long bonds and viceversa. This suggests that C_n R chains could have a radicalic character, with unpaired electrons located on the terminal carbon of the chain:



where “el” indicates the electrode. A further confirmation arises from the analysis of the bond lengths between the terminal carbon of the chain and the neighboring atoms, being, for C_{11} (C_{12}), 1.53 (1.56) Å the chain-electrode bond and about 1.37 (1.38) Å the bond with the second carbon of the chain. The latter turns out to be close to the $C - C$ bond length of 1.41 Å of bulk graphene and noticeably longer than the other interchain bond lengths.

Second, we investigated the dependence of the BLA on the chain length. In fig. 5.6-left we reported the BLA, calculated at the center of the chain, for chains from C_3 to C_{12} . Odd members feature a perfect cumulenic behavior at the center of the chain, with BLA values of ~ 0.02 and 0.04 pm for C_n and C_n R, respectively. As opposite, even chains show a polyynic structure, considerably more marked in C_n case, which become more cumulenic with the chain length as a consequence of the increased electron delocalization (π conjugation) throughout the backbone.

At last we focused on the contact geometry, examining the chain-electrode bond lengths, since they play a key role in determining the strength of the coupling. The results are shown in fig. 5.6-right, featuring bond lengths remarkably longer for C_n R chains, in average ~ 0.15 Å, if compared with C_n , as a consequence of the high strain of the four-atom ring. Moreover, even-odd oscillations can be observed in the bond length, reflecting the polyynic-cumulenic behavior of the chain.

We also studied the relative stability of the two geometries (see fig. 5.7), finding that

*the bond length alternation is defined as the difference between the lengths (d) of two consecutive bonds k and $k - 1$:

$$BLA_k = |d_k - d_{k-1}| \quad (5.2)$$

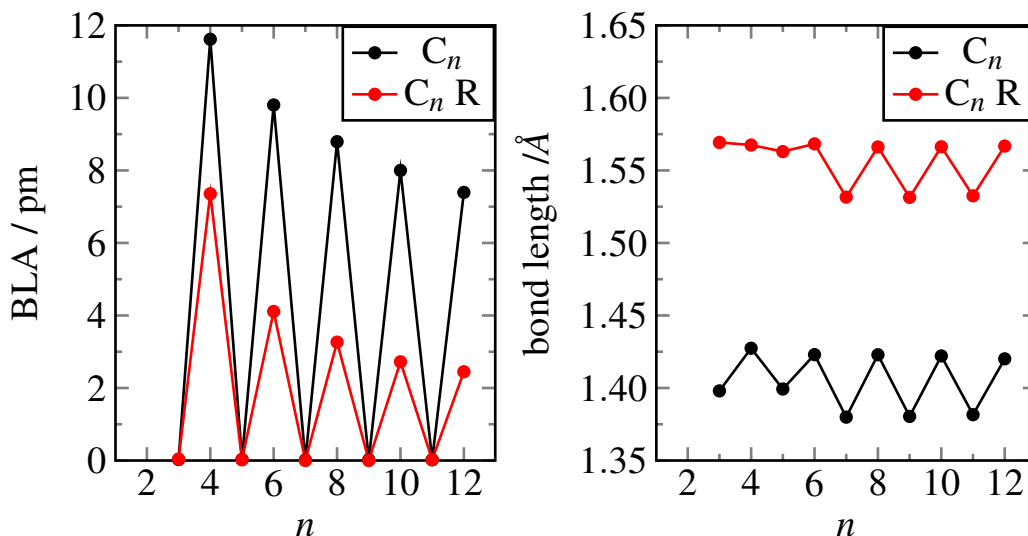


FIGURE 5.6: Left panel: bond length alternation calculated at the center of the molecule for C_n , $C_n R$ chains. Right panel: chain-electrode bond lengths for C_n , $C_n R$ chains

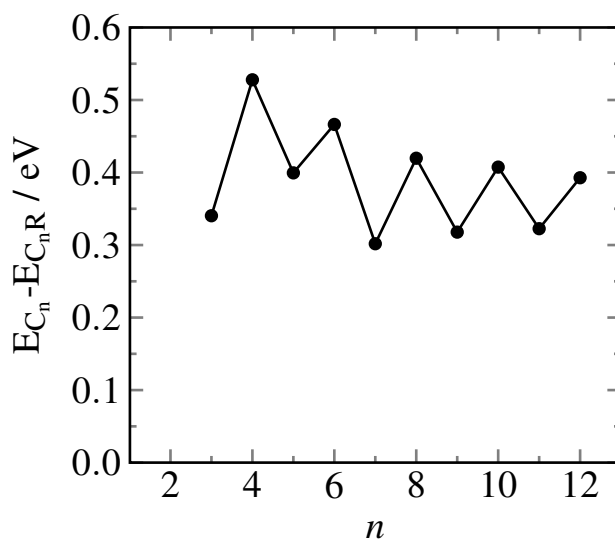


FIGURE 5.7: Energy differences (per contact) between C_n and $C_n R$ structures

the $C_n R$ are the most favored ones, especially in even members. Although those results are affected by basis-set superposition error (BSSE), which is different in the two configurations, we point out that the relatively small energy differences (< 0.6 eV) suggest that both structures can form in typical experimental setups. Of course this issue would require further investigations in the future.

Next we examined in details the electronic structure of C_7 and $C_7 R$ chains, in order to determine its relation with the geometric structure. In the following we will indicate with \perp the orbitals/states orthogonal to the electrode plane (the y direction of fig. 5.3) and with $//$ those along the edge direction (the x direction of fig. 5.3).

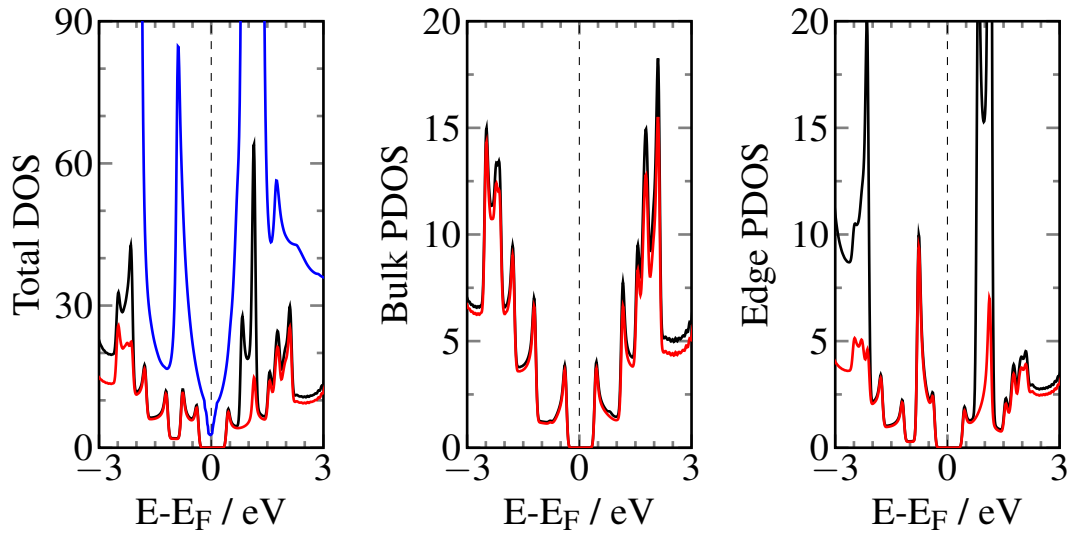


FIGURE 5.8: Density of states (majority spin) for the zigzag nanoribbon considered in the text. Left panel: total DOS (black) and projection onto the p_{\perp} orbitals (red) from electronic structure calculations with periodic boundary conditions. For comparison, also the total density of states for the semi-infinite system is reported (blue). Middle: total DOS (black) and its p_{\perp} projection (red) for bulk atoms. Right: total (black) and p_{\perp} -projected DOS (red) for edge atoms.

To this aim we performed electronic structure calculations in order to compute the density of states (DOS) of the system, focusing on its projection onto the p_{\perp} orbitals, being the most relevant in determining the transport properties. For such calculations we considered the same simulation cell used in the transport calculation (see fig. 5.3) with the nanoribbon edges either connected through a C_7 chain or separated by $\sim 13 \text{ \AA}$ of vacuum. It is worth highlighting that we are considering a rather different physical system, with respect to that adopted for the transport calculations. In fact in this case periodic boundary conditions are employed, effectively giving rise to nanoribbons of finite width (namely 8-ZGNR according with the common nomenclature[†]) separated by vacuum or connected through the chain. As opposite, in transport calculations, the system is semi-infinite in the transport direction, effectively giving rise to two semi-infinite graphene sheets separated by vacuum or connected through the chain. However this step has been necessary since many informations on the electronic structure of the system can not be extracted from transport calculations in a simple way, making difficult a deep understanding of the issues affecting the transport properties. However, under the assumption – justified a posteriori – that the binding of the chain mainly affects the edge states and does not induce deep changes in the bulk ones, many properties can be

[†] Armchair nanoribbons are classified by the number of dimer lines across the ribbon width, while zigzag nanoribbons by the number of zigzag chains across the ribbon width, in according *e.g.* with ref. [Dutta and Pati¹²⁷

also translated to the semi-infinite case.

The zigzag nanoribbon without the chain turns out to be semiconducting (see fig. 5.8), with a gap of ~ 0.6 eV at the Fermi level, and characterized by antiferromagnetic order. The density of states in the energy region considered is dominated by the π_{\perp} states and features a number of Van Hove singularities indicating the effective quantum confinement typical of monodimensional systems along the transport direction (z in fig. 5.3). Of course in the semi-infinite system the gap turn out to be closed, and the DOS in the Fermi level region resembles that of graphene.

The binding of the chain has relevant effects on the electronic structure of the nanoribbon. In fig. 5.10, we show the DOS projected onto the p_{\perp} orbitals of the edge (the outermost layer of the ribbon) and bulk (the regions depicted as electrodes in fig. 5.3) atoms for the nanoribbon with C_7 and without the chain, along with the p_{\parallel} and p_{\perp} projections on the chain atoms.

It appears evident the different chain-electrode coupling for the π_{\parallel} and π_{\perp} states of the chain. After binding the electrodes, the π_{\parallel} states remain localized in energy, indicating a weak coupling, except the one at ~ -2.5 eV, which broadens probably as a consequence of the interaction with the neighboring p_z orbitals of the edge hosting the unpaired electrons.

As opposite, π_{\perp} states strongly couple with the delocalized π electron cloud of graphene, resulting in broadened electronic states spanning almost all over the energy range considered. As a consequence of the strong coupling, each chain π_{\perp} state can hybridize with a large number of electrode states, giving rise to a number of electronic states delocalized on the whole system. In general such states remain close in energy but, in many cases, appear as resolved peaks in the DOS. For instance, this is particularly evident in the region $[-3.0, -1.5]$ eV, where four different electronic states, all involving the $HOMO_{-1}$ of the chain, can be easily identified. Thus, as a consequence of the similar strength of the chain and the electrode bonds, it turns out that the chain states loose their identity, *i.e.* it would be no longer correct to speak about “chain states” but rather one should refer to the “scattering-region states” (although in the description of the transport properties in some cases we will refer to the transmission resonances as originated by a single chain state, in order to simplify the discussion). This turns out to be one of the main differences between silver and graphene electrodes. In fact, with silver electrodes, the chain states, although considerably hybridized with the electrodes, maintain their individuality since the coupling is not strong enough to modify the geometric and electronic structure of the chain in a significative way.

With the help of the analysis of the Local Density of States (LDOS), we can group the

C_7		$C_7 R$	
energy range	chain state	energy range	chain state
[-4.0, -2.8] eV	$HOMO_{-2}$	[-4.0, -2.2] eV	$HOMO_{-2}$
[-2.8, -1.3] eV	$HOMO_{-1}$	[-2.2, -0.8] eV	$HOMO_{-1}$
[-1.3, 1.5] eV	$HOMO$	[-0.8, 0.9] eV	$HOMO$
[1.5, 2.3] eV	$LUMO$	[0.9, 2.2] eV	$LUMO$
[2.3, 4.0] eV	$LUMO_{+1}$	[2.2, 4.0] eV	$LUMO_{+1}$

FIGURE 5.9: Energy ranges corresponding to the different chain states.

electronic states in which a given π_{\perp} state of the chain is involved as reported in fig. 5.9.

Analyzing the DOS projections on the edge and bulk atoms, it is also evident that the binding of the chain significantly affects the edge states, especially those closer to the Fermi level, while introduces minor modifications in the bulk states, if compared with the ribbon without chain. In particular edge and bulk states are introduced in the gap in correspondence of the π_{\perp} chain state right at the Fermi level, providing further indications that the electronic states do not extend on the chain only. However in this specific case the contribution of bulk states is negligible, thus this state is expected to be poorly conductive since it is mainly localized on the chain ($HOMO$) and on the edge only.

The other electronic states closer to the Fermi level, again involving the $HOMO$, are more broadened in energy and feature a very large contribution of edge state as well as a non-negligible contribution of bulk states.

In the other regions of the DOS, the electronic states involving $HOMO_{-1}$, $HOMO_{-2}$, $LUMO$ and $LUMO_{+1}$ turn out to be highly spread in energy, resulting in a continuous of states highly hybridized with the edge and extending also on the bulk region.

$C_7 R$ behaves similarly, but the longer chain-electrode bonds (1.53 Å vs 1.38 Å of C_7) determine a weaker coupling of π_{\perp} chain states with the electrodes – although this is partially compensated by the presence of two chain-electrode bonds – if compared with C_7 . As a result π_{\perp} chain states turn out to be less broadened and shifted toward the Fermi level. Furthermore the integration of the projected DOS have revealed that 0.8 electrons are transferred from the π_{\parallel} to the σ states of the chain, indicating that the chain-electrode bonds feature a prevalent σ character. The binding of the chain also introduces significative modification in the edge states, in particular the π_{\perp} chain states close to the Fermi level turn out to be considerably more hybridized with the edge ones, with respect to C_7 . However, also in this case, the bulk states are not deeply affected by the binding of the chain.

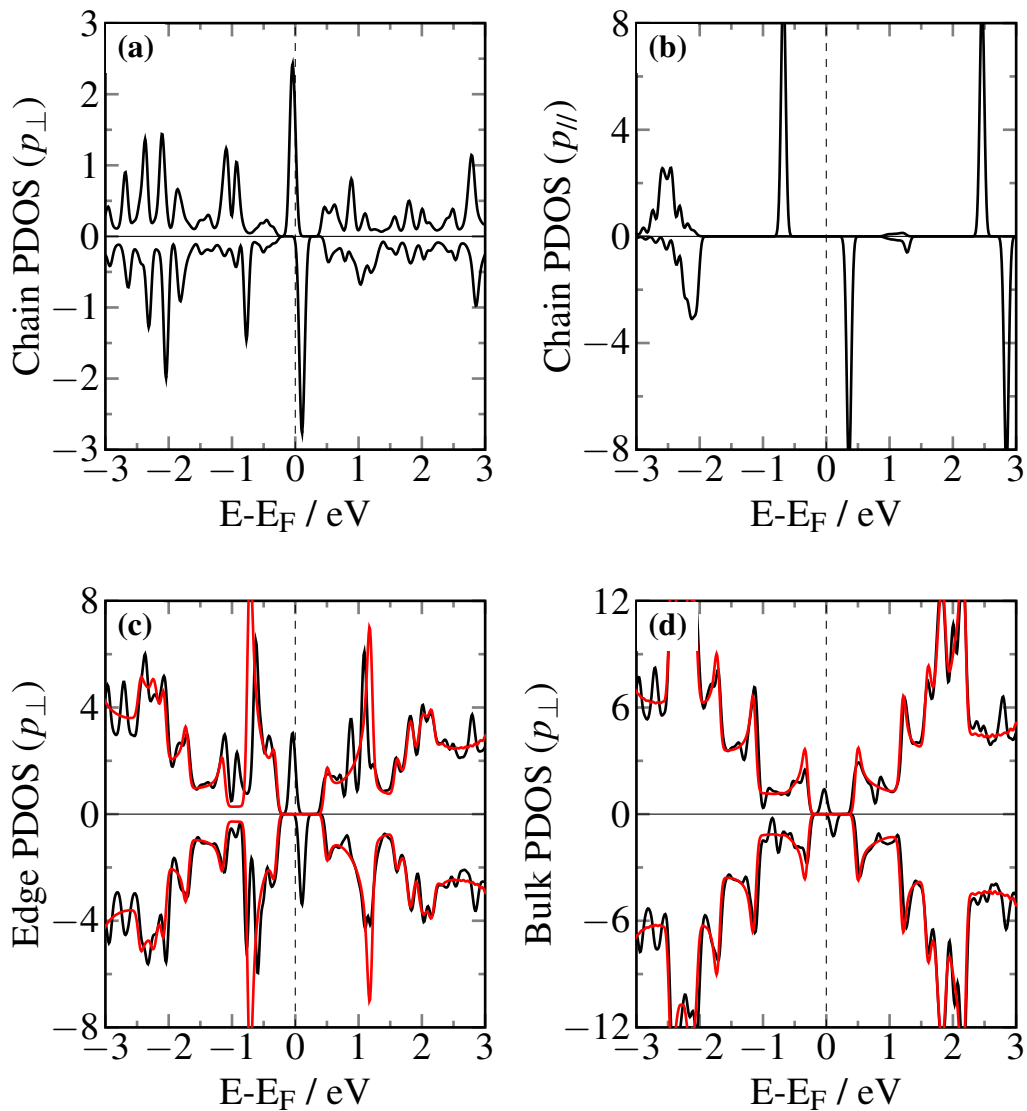


FIGURE 5.10: Density of states for the zig-zag nanoribbon connected through a C_7 chain (black) and without chain (red). Results have been portrayed for spin majority (upper curves) and spin minority (lower curves) components. (a) DOS projection onto the p_{\perp} orbitals of the chain. (b) DOS projection onto the p_{\parallel} orbitals of the chain. (c) p_{\perp} -projected DOS for edge atoms. (d) p_{\perp} -projected DOS for bulk atoms.

The transmission probabilities reflect the results explained above. We highlight again that transport calculations refer to a different physical system with respect to those previously described (semi-infinite *vs* periodic), however we found a good agreement between the position of the states in the above DOS and the resonances in the transmission spectra, strengthening the idea that many issues, concerning *e. g.* the relation between junction geometry and electronic structure, can be extended to the semi-infinite system. Thus in the following we assume an implicit relationship between the resonances and the electronic states provided by the DOS calculations.

In these systems, only the π_{\perp} states of the chain hold the conduction process, *i.e.* deter-

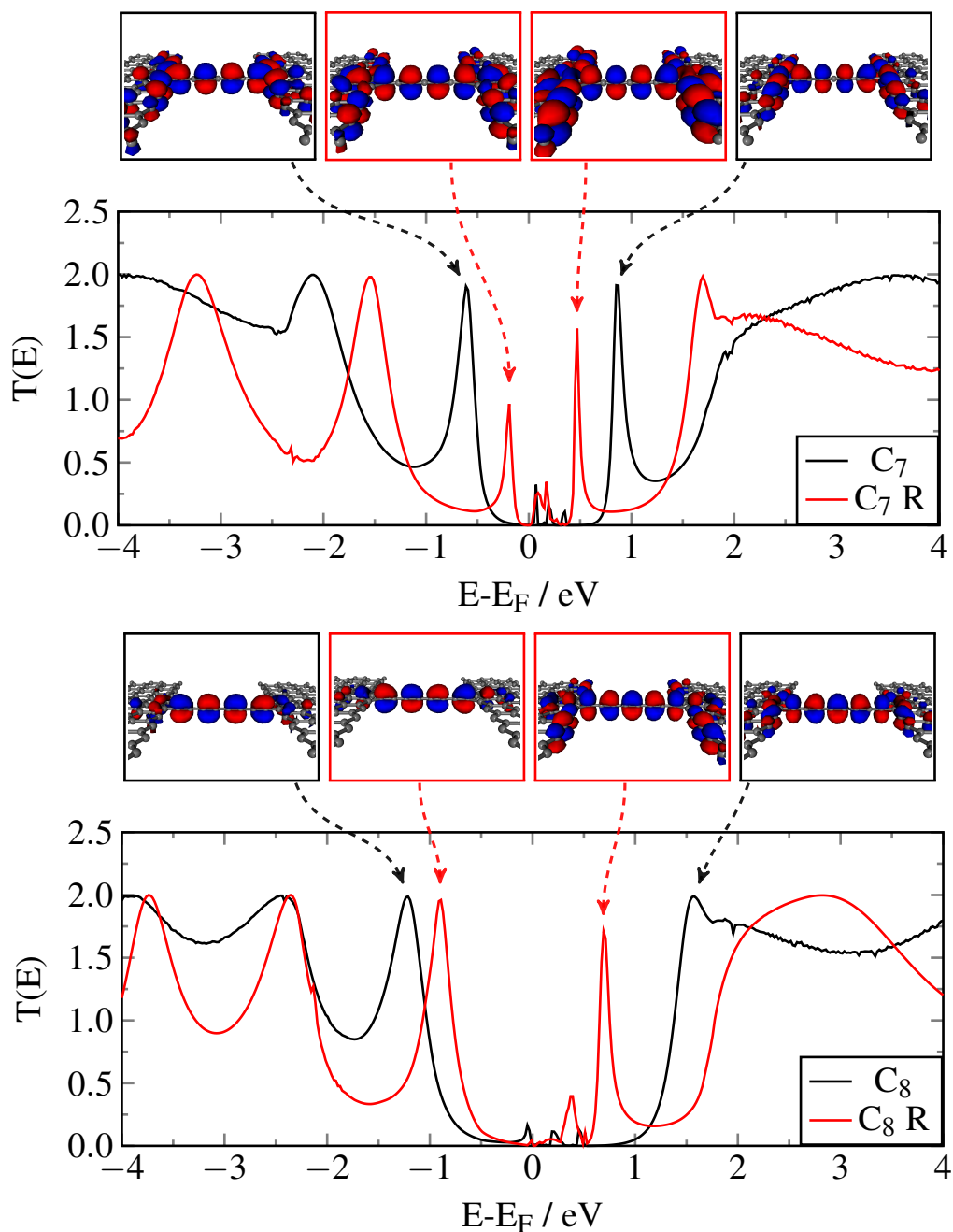


FIGURE 5.11: Transmission of C_7 , C_8 and corresponding R chains. Some selected eigenchannels are reported above the plots.

mine the resonances in the transmission spectra, giving rise to a maximum theoretical transmission value of 2 (taking into account the spin).

The two junction geometries feature very different transmission spectra, as shown in fig. 5.11 for the C_7 case. C_7 shows two relatively narrow resonances at ~ -0.7 and ~ 0.9 eV, separated by a non-conductive region. The computation of the eigenchannels shows that both electronic states giving rise to such resonances involve the *HOMO* of the chain (see fig. 5.11, black boxes above the top plot). The regions below -1.2

eV and above 1.5 eV feature very large and unresolved resonances, indicating that the corresponding states strongly couples with the electrode bulk states, in agreement with the results explained above. It follows that such states are highly conductive, providing transmission values close to the maximum allowed.

In the C_7 R case, it is evident that the weak chain-electrode coupling causes a significant narrowing of the resonances, giving rise to more resolved peaks in the transmission spectrum, compared to C_7 . Moreover we noticed a significant shift of the resonances toward the Fermi level. Clearly this is a direct consequence of the weak coupling which remarkably reduce the broadening of the *HOMO*. As a result the two “*HOMO*” resonances of C_7 shift to -0.25 and 0.5 eV in C_7 R, as confirmed by eigenchannel calculations (see fig. 5.11, red boxes above the top plot), considerably narrowing and decreasing in magnitude.

We also compared the transmission of C_8 and C_8 R, as shown in fig. 5.11. Also in this case the different coupling induces remarkable differences between the transmission spectra. C_8 spectrum features in general non-resolved resonances and a large non-conductive gap between those closer to the Fermi level, which turn out to involve the *HOMO* (~ -1.2 eV) and *LUMO* (~ 1.5 eV) states as results from eigenchannel analysis (fig. 5.11, black boxes above the bottom plot). The more cumulenic character of C_8 R chain causes the *HOMO-LUMO* gap to reduce, leading the resonances to approach the Fermi level. Moreover the weaker coupling considerably narrows the resonances, in particular the “*LUMO*” one (~ 0.7 eV) turns out to be well-resolved.

We further analyzed in details the behavior of the low-transmission gap in the Fermi level region and the width of the resonances closest to the Fermi level as a function of the chain length. The low-transmission gap has been calculated as the difference between the maxima of the two “*HOMO*” resonances for odd chains and between the maxima of the “*HOMO*” and “*LUMO*” resonances for even chains. The results are summarized in fig. 5.12. It is evident that the transmission gap strongly relates with the polyynic/cumulenic character of the chain (see fig. 5.6). Even C_n chains feature a significant polyynic character, hence a large *HOMO-LUMO* gap, resulting in the largest transmission gap values. Even C_n R chains are more cumulenic, causing the *HOMO-LUMO* gap, and in turn the transmission gap, to reduce. Odd chains feature a state at the Fermi level which turns out to be localized only on the chain and on the electrode edge, resulting non-conductive. Thus the transmission gap turns out to be related to the gap between the two conductive states closest to the Fermi level, and the different behavior between C_n and C_n R mainly relates to the different chain-electrode coupling, *i.e.* with the different broadening of the *HOMO* state.

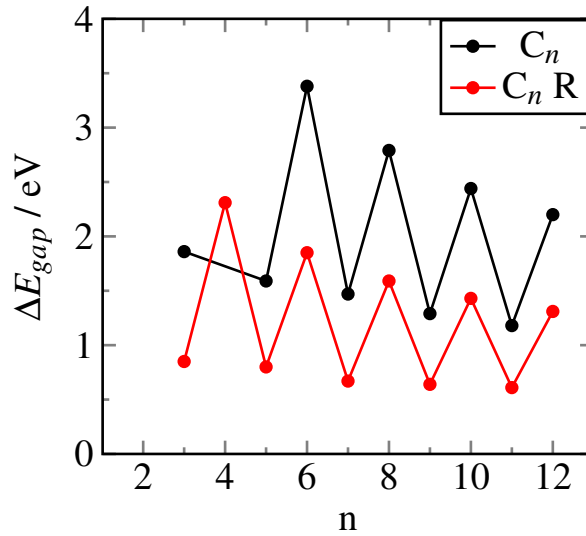
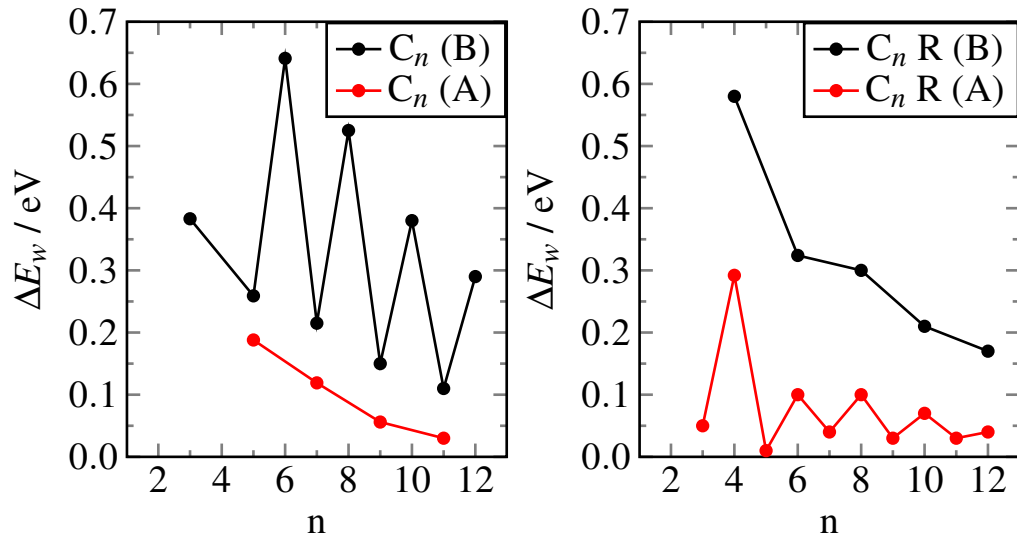


FIGURE 5.12: Energy gap between the resonances closest to the Fermi level.

FIGURE 5.13: Left panel: Width of the first resonance below (B) and above (A) the Fermi level for C_n chains calculated where $T(E)=1$. Right panel: As left panel for $C_n R$ chains. See text for details.

In all cases, the transmission gap decreases with the chain length as a consequence of the increasing in the π conjugation of the chain.

We further analyzed the width of the first resonance above (A) and below (B) the Fermi level, calculated (when possible) for $T(E)=1$, as a function of the chain length. The results are reported in fig. 5.13. For C_n chains, the B resonance width features significant even-odd oscillations, with even chains providing the larger widths. This implies a different coupling between the corresponding states and the electrodes, much stronger for even chains. For the resonance A we can extract only the widths for odd chains (for even chains this resonance is not resolved), which turn out to be slightly smaller

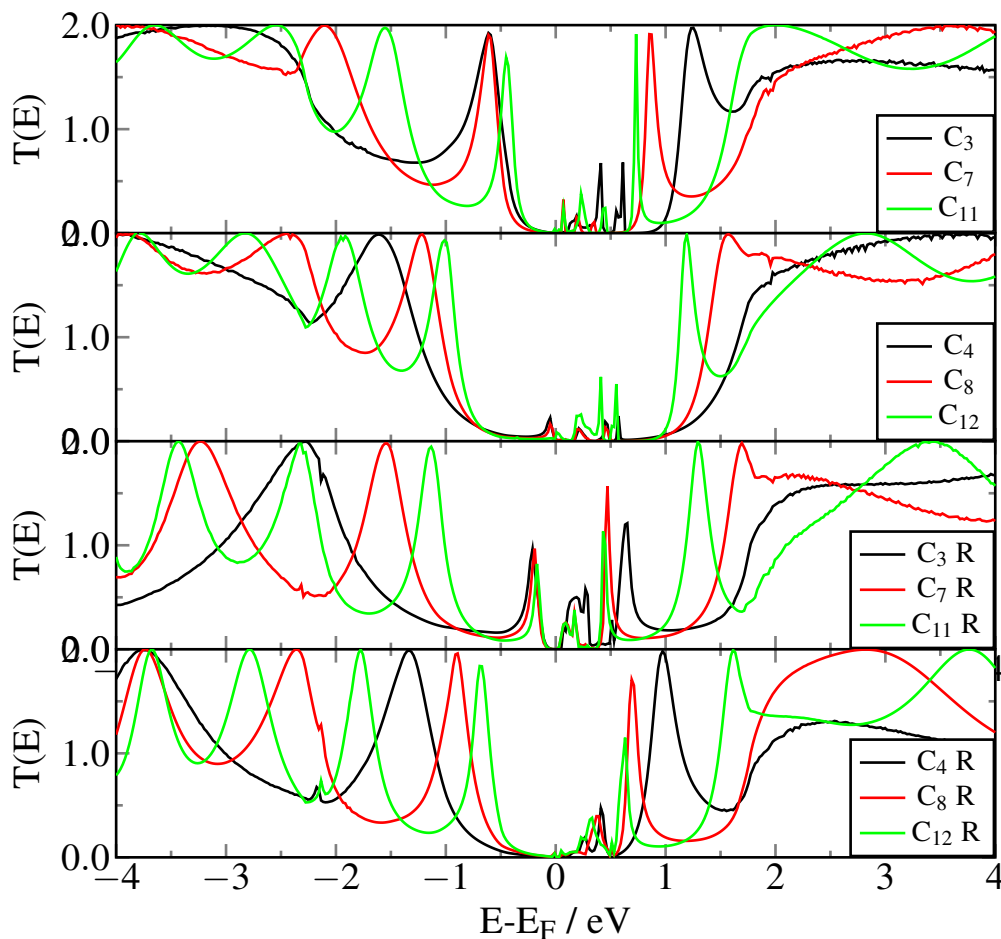


FIGURE 5.14: Transmission spectra of some selected C_n and C_n R chains.

that these of resonance B, indicating a slightly weaker coupling. For C_n R chains, the resonance B in even chains provides width values only slightly lower with respect to the C_n case, indicating couplings of similar magnitude. This is an unexpected behavior, since the longer chain-electrode bond lengths would result in a remarkable narrowing of the resonances, however we argued that the presence of two chain-electrode bonds partially compensates the increased bond lengths. In odd members the magnitude of the resonance B is lower than one, preventing us to perform this simple analysis. Remarkably more different is the behavior of the resonance A, featuring, in odd members, widths almost independent on the chain length and considerably lower with respect to C_n ones, although both seem to tend to the same value with the chain length.

Finally we summarize the results explained above analyzing the transmission spectra for different chain length and junction configuration as reported in fig. 5.14.

In general even C_n chains show a large window between the *HOMO* and *LUMO* resonances characterized by very low transmission probabilities, due to the lack of conductive states in this region, except for some state arising from the broadening of the

HOMO and *LUMO* generating very weak resonances. This window only slightly reduces with the chain length as a consequence of the reduction of the *HOMO-LUMO* gap due to the increased π conjugation of the chain.

The increased cumulenic behavior of even C_n R chains lead to a significant reduction of the *HOMO-LUMO* gap, causing a general shift of all π_{\perp} chain states toward the Fermi level. For instance, this is particularly evident for the $HOMO_{-1}$ resonance, being shifted from -3.8 eV for C_4 R to -1.8 eV for C_{12} R. Moreover the reduced chain-electrode coupling determines a significant narrowing of all resonances.

Odd C_n chains feature a reduction of the low-transmission window with respect to even members, due to their cumulenic structure. Such window reduces from ~ 1.8 eV for C_3 to ~ 1.2 eV for C_{11} because the *HOMO* resonance above the Fermi level is shifted downwards in energy while the one below the Fermi level is unaffected by the chain length.

Odd C_n TS4 chains behave similarly, but, the reduced chain-electrode coupling with respect to C_n causes the resonances to considerably narrow and approach the Fermi level. Specifically the reduction of the broadening of the *HOMO* causes an increasing of the DOS and, in turn, of the transmission, in the region between the two “HOMO” resonances.

5.2.2 Tips

In this section we investigate more in details the effects the contact geometry plays in determining the transport properties, focusing on C_3 and C_4 chains, chosen as representative of odd and even members, connected to the electrodes through tips (see fig. 5.15). To this aim we considered symmetric systems, where the chain is connected to the edges either through pentagonal tips (C_n P), with a junction configuration resembling that of an armchair-bound chain, or through triangular tips with 1, 2 or 3 benzenic rings along the edge (C_n 1T, 2T and 3T, respectively).

Pentagonal tips

First we focus in details on the C_3 P structure. The pentagonal tips moderately modify the chain geometry as a consequence of the strain induced by the pentagonal ring, whose atoms tend to achieve a sp^2 hybridization. In fact, while C_3 is perfectly linear, the pentagonal tip induces a chain distortion in the electrode plane, with the three atoms forming an angle of 171.45° , and both the interchain and the chain-electrode bonds

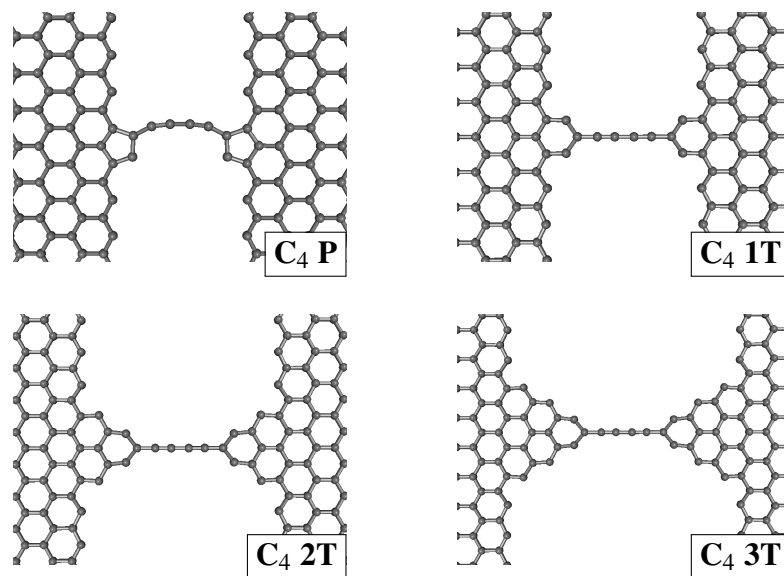


FIGURE 5.15: Structures of tips

turns out to be slightly stretched by $\sim 0.03 \text{ \AA}$.

On the other hand significant changes occur in the electronic structure and hence in the transport properties. As in the previous section, we first analyze the π_{\perp} projections on chain, bulk, edge and tips atoms, reported in fig. 5.16 along with the corresponding results obtained for C_3 directly contacted with the zigzag edge. It is evident a general shift of the DOS upwards in energy, indicating a general destabilization of π_{\perp} states with respect to C_3 , probably induced by the residual strain of the pentagonal ring and by the consequent distortion of the chain. However no significant differences have been found in the charge transfer from the π_{\perp} to the σ states of edge and bulk in the two structures, being 0.075 and 0.05 $|e|/\text{atom}$, respectively, for both cases. We only noticed a small change in the $\pi_{\perp} \rightarrow \sigma$ charge transfer for chain atoms, with 0.02 and 0.035 $|e|/\text{atom}$ transferred for C_3 and $C_3 \text{ P}$, respectively. Hence, such results suggest that no states cross the Fermi level.

The DOS of C_3 parallel that of C_7 presented in the previous section, in particular showing a chain state at the Fermi level which is strongly hybridized with edge states only. In the $C_3 \text{ P}$ structure, this state considerably couples with the tips, and consequently broadens.

Those findings nicely relates with the results obtained by transport calculations. The transmission spectrum of C_3 (see fig.5.17) features two ‘‘HOMO’’ resonances at -0.6 and 1.2 eV and two wide resonances below -2 eV and above 1.7 eV originated by the $HOMO_{-1}$ and $LUMO$ states, respectively. In $C_3 \text{ P}$, several effects has to be taken into

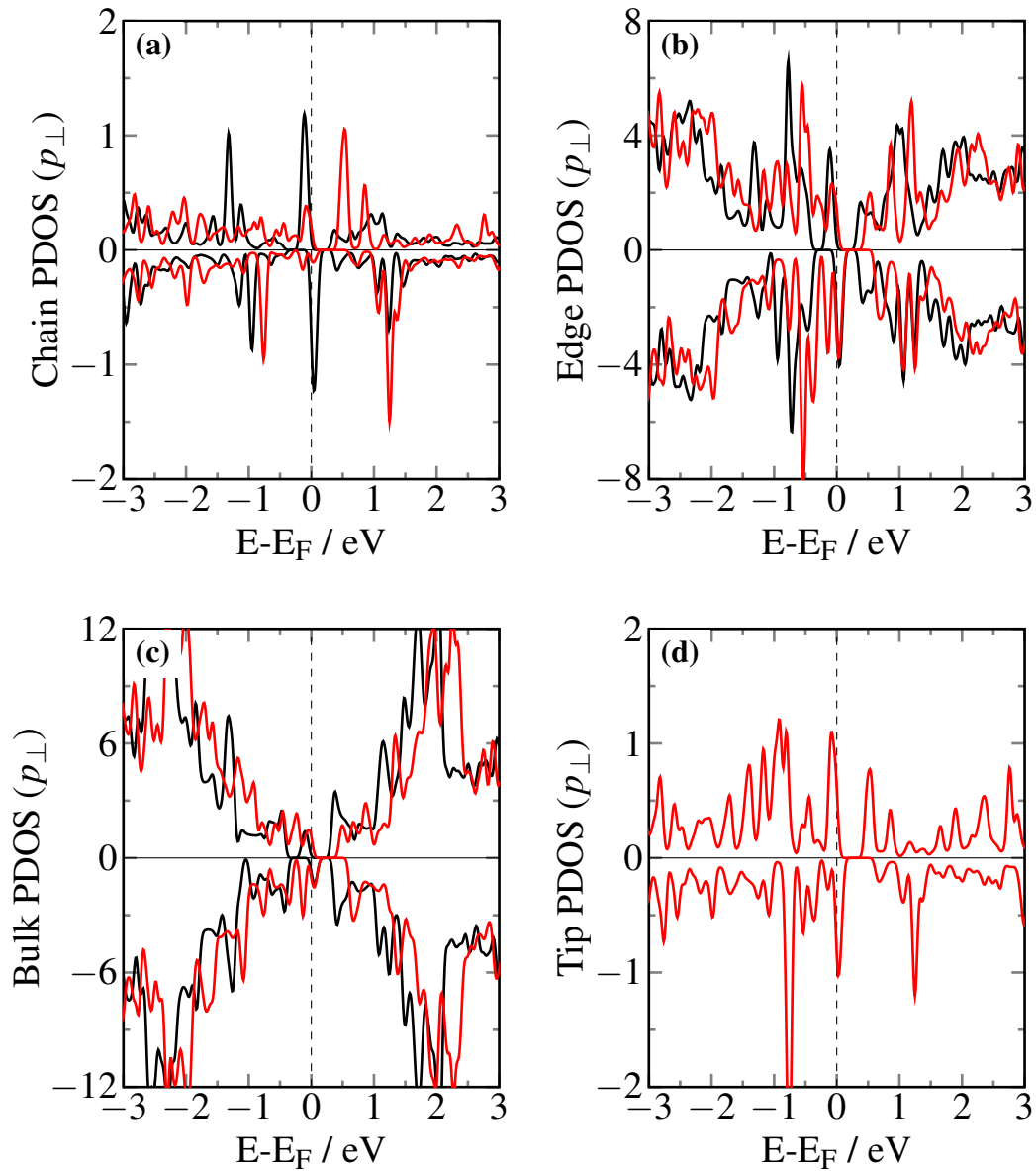


FIGURE 5.16: Density of states for a C_3 chain connected with the zig-zag nanoribbon without tips (black) and through pentagonal tips (red). Results have been portrayed for spin majority (upper curves) and spin minority (lower curves) components. (a) DOS projection onto the p_{\perp} orbitals of the chain. (b) p_{\perp} -projected DOS for edge atoms. (c) p_{\perp} -projected DOS for bulk atoms. (d) p_{\perp} -projected DOS for tip atoms.

account to explain the completely different transmission spectrum. First, the destabilization of π_{\perp} states lead to a general shift of all states at higher energies. The only exception is the “*HOMO*” resonance above the Fermi level, whose position and magnitude turn out to be irrespective of the different junction geometry, while the one below the Fermi level moves to ~ -0.2 eV, considerably narrowing and decreasing in magnitude. Second, the tips increase the π conjugation of the chain, introducing further π states and, then, further resonances in the transmission spectrum. As a consequence the

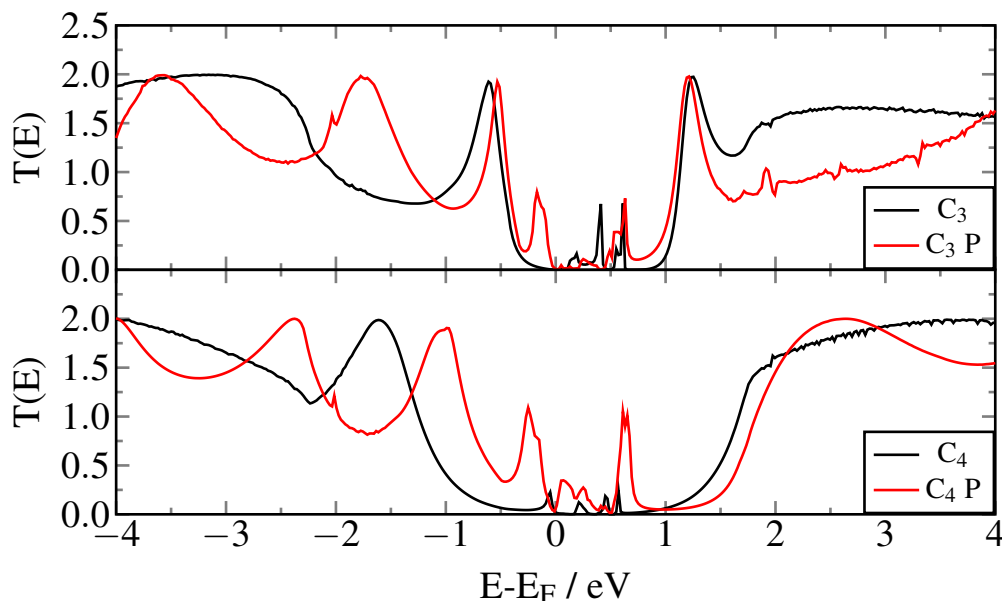


FIGURE 5.17: Transmission spectra of C_3 and C_3 P chains (top) and of C_4 and C_4 P chains (bottom).

resonances narrow and approach the Fermi level. Third, the strain of the chain and of the chain-electrode bonds further contributes to the sizable narrowing of the resonances, with respect to C_3 .

We observed a similar behavior for C_4 P, as shown in fig. 5.17. In this case minor changes in the chain geometry occur with respect to the previous case. Compared with C_4 , the chain turns out to be slightly more cumulenic – the BLA decreases by 0.01 \AA – and slight bent in the electrode plane as a consequence of the sp^2 hybridization of the contacting atoms of the tips. The spectrum of C_4 feature a large weakly conductive window between the wide resonances originated by *HOMO* ($\sim -1.8 \text{ eV}$) and *LUMO* (above 1.5 eV) states. In C_4 P, the destabilization induced by the tips causes a general shift of the occupied π_{\perp} states at higher energies, causing the *HOMO* state to partially deplete and cross the Fermi level, giving rise to two well-separated weak resonances at -0.25 and 0.6 eV .

Triangular tips

Here we consider triangular tips of different size. In this case the tip induces more dramatic effect in the the DOS and in the transmission of the system, with respect to the previous case. The results turn out to be almost independent on the tip size. First, as in the previous cases, the tips induce a destabilization of the system, causing all π_{\perp} states to shift upwards in energy. Second, the π_{\perp} *HOMO* state turn out to be hybridized with the tips only, hence completely decoupled from the electrodes. Of course, this has

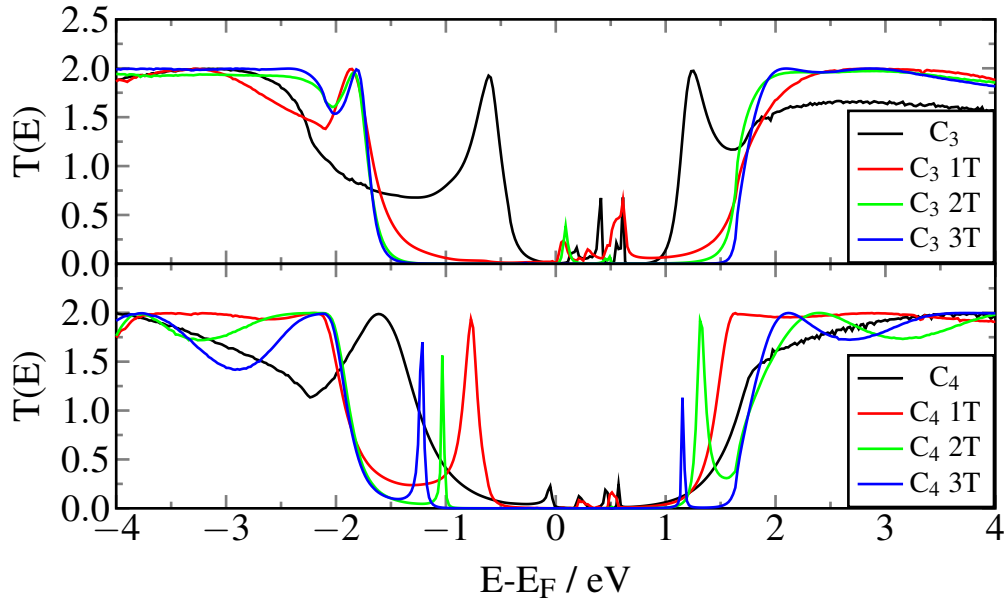


FIGURE 5.18: Transmission spectra of C_3 and C_4 contacted with triangular tips.

relevant effects on the transmission function (see fig. 5.18), giving rise to a very large non-conductive window from -1.5 to 1.5 eV. As opposite, the states below -1.5 eV and above 1.5 eV turns out to be perfectly conductive, giving rise to step-like resonances with transmission values close to the maximum allowed for this system.

Moreover also C_4 behaves similarly, featuring a drastic reduction of the coupling of the *HOMO* and *LUMO* with bulk states (fig. 5.18). However these states turn out to be weakly conductive and generate narrow resonances in the transmission spectrum. Such resonances shift downwards in energy and slightly drift apart by increasing the tip size. For instance for C_4 1T the *LUMO* resonance lies at 1.5 eV – although it is not resolved – while for C_4 3T it is found at 1.2 eV. Otherwise the *HOMO* resonance lies at -0.8 and -1.3 eV for C_4 1T and 3T, respectively. Moreover such resonances considerably narrows by increasing the tip size. However this behavior is certainly not related to changes in the chain geometry, that we found being irrespective on the tip size, but we argued that, increasing the dimension of the tip, such states are progressively less destabilized, moving at lower energies, and less coupled with the electrodes, explaining the reduction of the resonance width.

5.2.3 Double chains

The characteristics of nanoscale devices are mainly determined by quantum-mechanical effects, which can give rise to behaviors without classical equivalents. Among these

effects, quantum interference has been suggested for the implementation of molecular switches^{128–130}, logic gates¹³¹ and data storage elements¹³².

Quantum interference effects have been studied in phase-coherent mesoscopic systems for decades. The classic example is an Aharonov-Bohm (AB) metallic ring, where an electron wave coming from the left contact splits, follows two paths A and B and then can interfere on the right contact¹³³. The interference pattern can be switched from constructive to destructive by applying a magnetic field through the ring, because the electron waves traveling through A will accumulate a different phase than those traveling through B. Overall, interference leads to oscillations in the electrical resistance as a function of the externally applied magnetic field B , with period $\Delta B = h/(eA)$, where h is Planck's constant, e is the elementary charge and A is the area of the ring. In these types of experiments, quantum interference is present as long as the phase-coherence length of the electron wave is comparable to the dimensions of the ring. Inelastic scattering would lead to phase-randomization and thus to the suppression of quantum mechanical effects.

Concerning molecules, benzene can be considered as the ultimate limit of miniaturization of an AB ring. However, the magnetic field required to observe AB oscillations is extremely high ($B \sim 10kT$). Nonetheless, interference effects can play a more subtle role in the electronic conduction by changing the intra-molecular current paths, which in turn deeply affect the electron transmission through the molecule.

In the last years many efforts have been carried out to understand this issue. In particular, many theoretical studies reported quantum interference effects in conjugated molecules^{128,134,135} and aromatic hydrocarbon systems^{136–138}. For example, Baer *et al.*¹²⁸ investigated, at tight-binding level of theory, several cross-linked molecular wire configurations, finding dramatic differences on the transport properties depending on their connectivity. Moreover they found that conductivity is mainly determined by the electron dynamics at the Fermi level where their wavelength is four multiples of the C-C bond length. Thus configurations with cross-linked distance equal to four bond lengths exhibit constructive interference, otherwise destructive interference.

The basic idea exploited by this model is that when multiple paths are available for conduction, electron passing through the molecules from one electrode to the other can either remain phase-coherent or not depending on the length of the channels and on the configuration of the system. In principle this could give rise to quantum interference effects, that can be described in terms of the interference pattern of the De Broglie waves associated to the electrons traveling through the molecules.

In this section we consider the possibility to observe interference patterns in double

chains connected to zigzag electrodes at different interchain distances, primarily focusing on elucidating the conditions for the appearance of constructive or destructive interference and on determining its effect on the transport properties.

To this aim we considered double C_3 , C_4 and C_8 chains distanced by a different number of zigzag units (indicated with nZ) along the electrode's edge. The structures are shown, for the C_4 case, in fig. 5.19. The case of double R chains as well as non-parallel C_4 chains will also be briefly addressed.

Double C_3 chains

Let's consider first double C_3 chains. Optimized double C_3 geometries show perfectly linear chains, except for C_3 1Z, where the central atoms point toward each other, bending the chains in the electrodic plane with an angle of 164.2° , as a consequence of the interchain interaction.

All the configurations considered show remarkable modifications in the transmission spectrum with respect to that of double non-interacting C_3 chains, obtained by doubling the transmission of the single chain, especially in the region $[-1.5, +1.5]$ eV, as shown in fig. 5.20 (top panel).

C_3 2Z, 3Z and 4Z behave similarly, featuring a splitting of the two *HOMO* resonances of the single chain into two peaks, with the one closer to the Fermi level of lower magnitude. For instance, in C_3 2Z the peak of C_3 at -0.6 eV splits into the resonances at -0.3 and -1 eV, the one at 1.25 eV into the resonances at 0.85 and 1.5 eV. Such resonances approach to each other by increasing the interchain separation but in C_3 4Z are still slightly visible. This effect results in a constructive interference pattern, reducing of the low-transmission window in the Fermi level region.

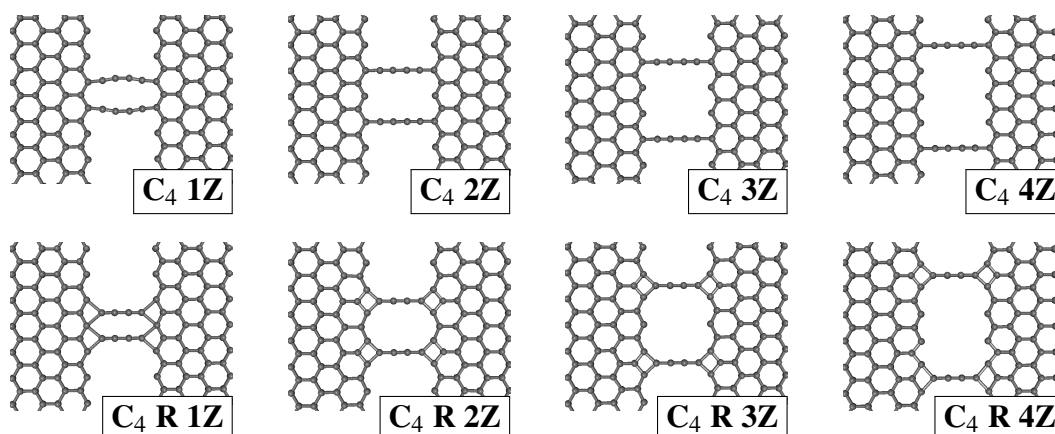


FIGURE 5.19: Structures of double C_4 chains

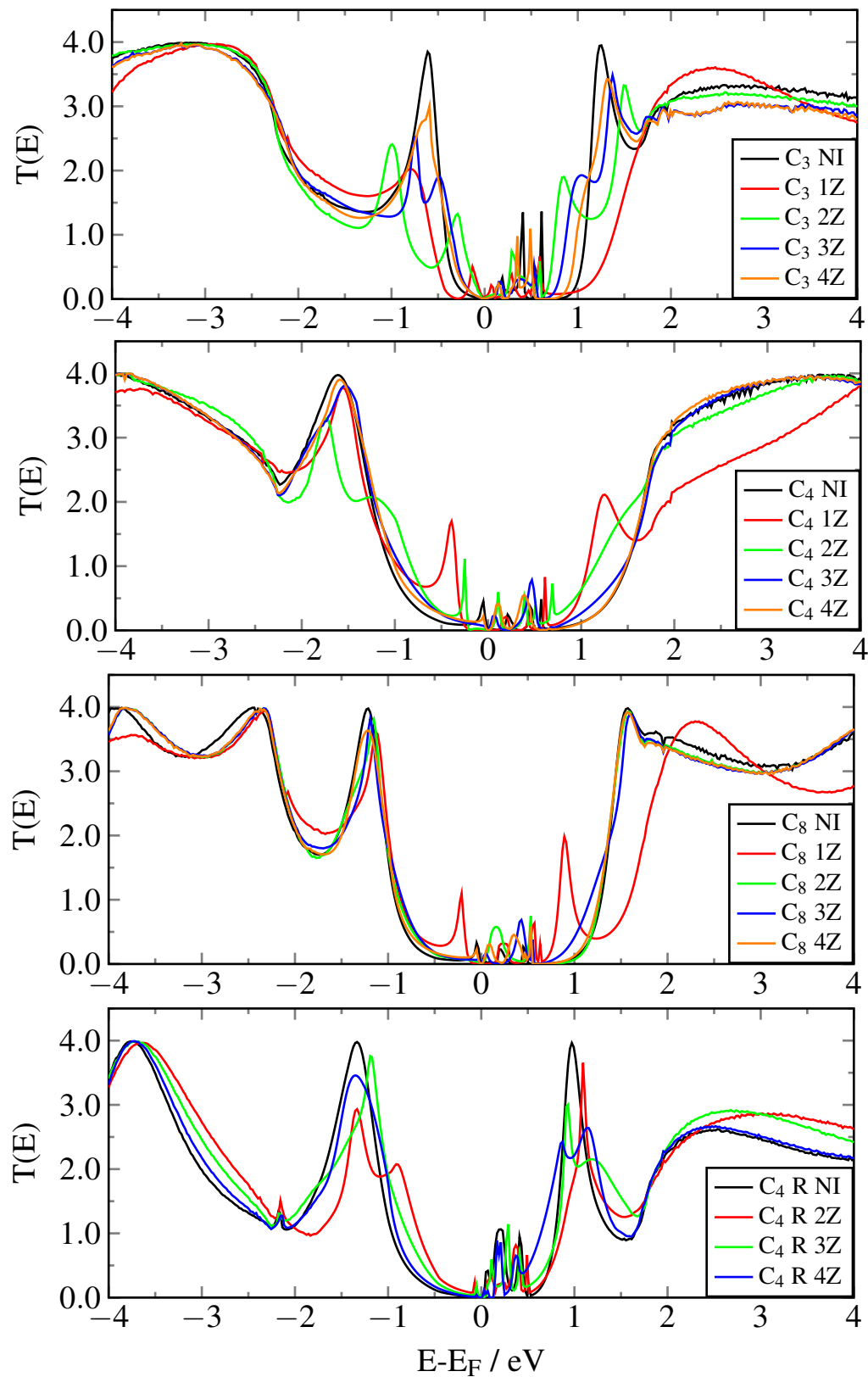


FIGURE 5.20: From top to bottom: transmission spectra of double C₃, C₄, C₈ and C₄ R chains. The transmission spectrum of the corresponding non-interacting (NI) double chains is also reported for comparison.

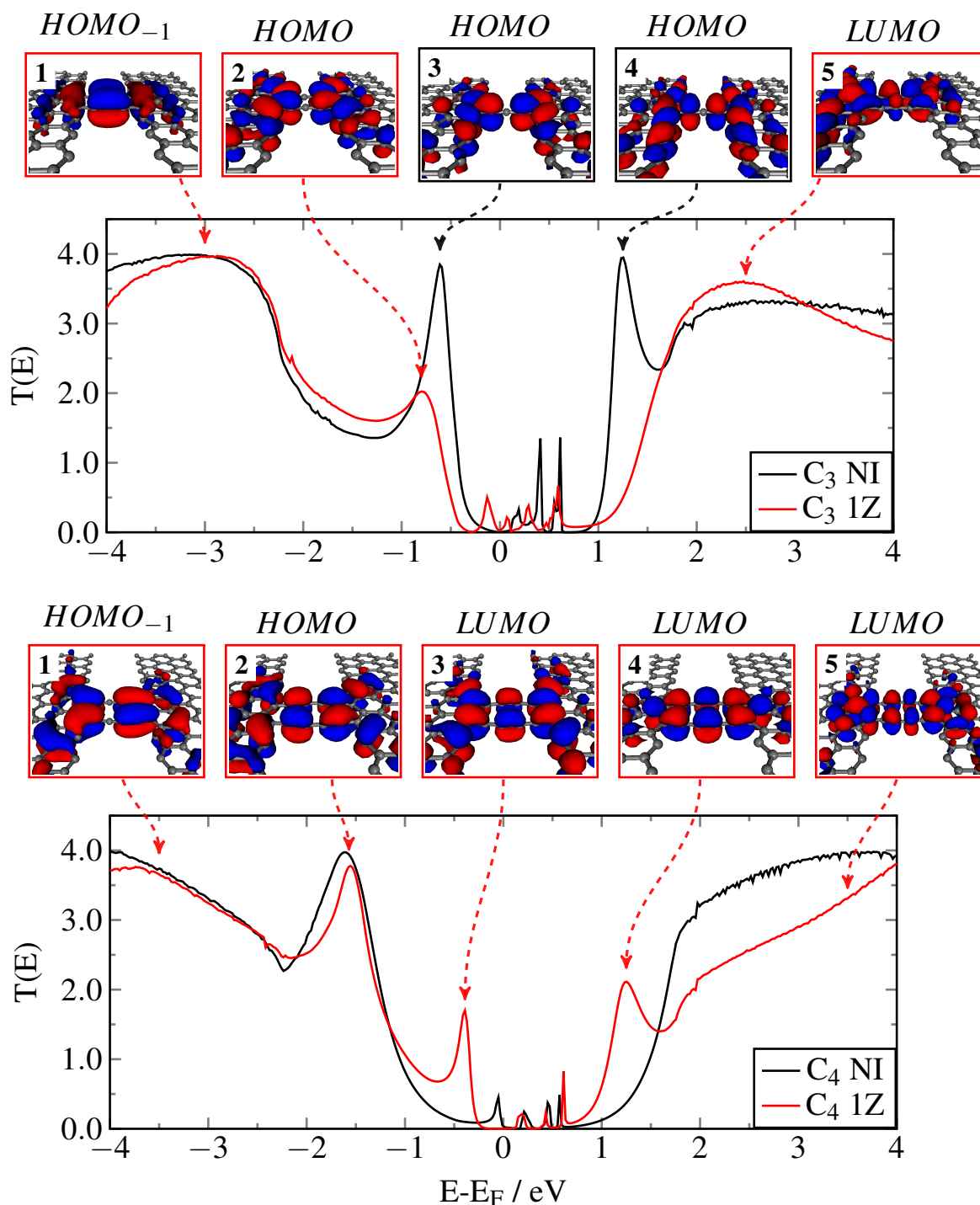


FIGURE 5.21: Top: transmission of non-interacting (NI) C_3 and C_3 1Z chains. Bottom: as top panel for C_4 chains. Above the plots the pictures of some selected eigenchannels are reported.

Completely different is the behavior of C_3 1Z, showing a drastic reduction of the transmission of the $HOMO$ and causing an enlargement of the low-transmission window in the Fermi energy region (see fig. 5.21). An accurate analysis of the chain projected DOS revealed that the $HOMO$ state giving rise to the resonance below the Fermi level

is shifted downwards in energy by ~ 0.2 eV and, mainly, results weaker coupled with the electrodes, when compared either with the single C_3 or with the C_3 4Z, explaining the magnitude halving of the corresponding transmission peak. On the other hand we found that the *HOMO* state above the Fermi level is shifted upwards in energy, merging with the *LUMO* state. Thus the interaction between double C_3 1Z chains results in a distancing of the *HOMO* resonances from the Fermi level, hence in a destructive interference effect that reduces the transmission probabilities in the Fermi level region.

Double C_4 chains

Next we considered double C_4 chains. As in the previous case the optimized structures feature linear chains, except for C_4 1Z where the chains are slightly bent in opposite directions because of the steric interchain repulsion interaction.

The transmission spectra of double C_4 chains are shown in fig. 5.20 (second panel). In this case the transmission spectra differ from the non-interacting chain one only for C_4 1Z and 2Z, while for more distanced chains no significative changes has been found.

Specifically C_4 1Z spectrum features two more resonances at about -0.45 and 1.25 eV with respect to non-interacting case, associated with a reduction of the transmission probabilities of the *LUMO* state. Analyzing the chain projected DOS we found a general lowering in energy of the *LUMO* state, which partially broadens also below the Fermi level and which is responsible for the formation of the two extra resonances, as confirmed by eigenchannels calculations (see fig. 5.21). This is associated with a self-doping process causing a partial electron transfer from the *HOMO* to the *LUMO* – $\sim 0.5 |e|$ from integration of the projected DOS – and a small charge transfer from the terminal atoms of the chains to the electrodes ($\sim 0.05 |e|$ per atom). Thus the *HOMO* partially depletes, giving rise to a state in the chain projected DOS at ~ 0.6 eV, which generates a very weak resonance in the transmission spectrum at the same energy.

As for double C_3 chains, 2Z configuration features a completely different behavior, showing a splitting of the *HOMO* resonance (located at ~ -1.6 eV for non-interacting chains case) into two peaks at about -1.75 and -1.25 eV as well as a not resolved splitting of the *LUMO* resonance. Also in this case we found a minor self-doping effect with transfer of $\sim 0.2 |e|$ from the *HOMO* to the *LUMO*, being responsible for the low-magnitude resonances at 0.1 and -0.25 eV, respectively, and a small charge transfer from the chains to the electrodes ($\sim 0.1 |e|$ per chain)

Double C_8 chains

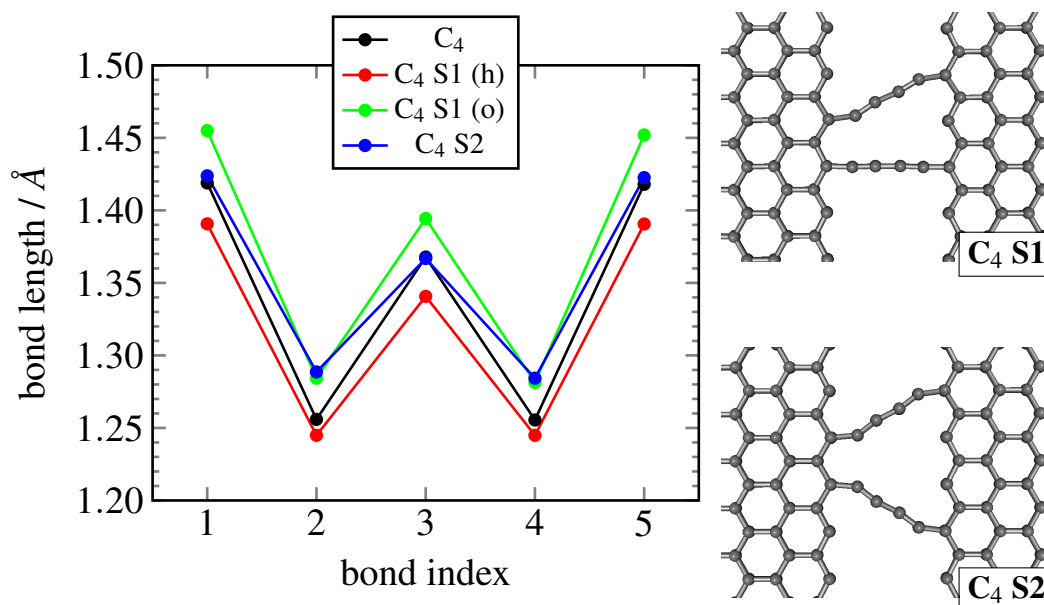


FIGURE 5.22: Structures and bond lengths of C_4 S1 (h=horizontal chain, o=oblique chain) and C_4 S2. The bond lengths of single C_4 chain are also shown for comparison. The bond indexes 1 and 5 are referred to the chain-electrode bond.

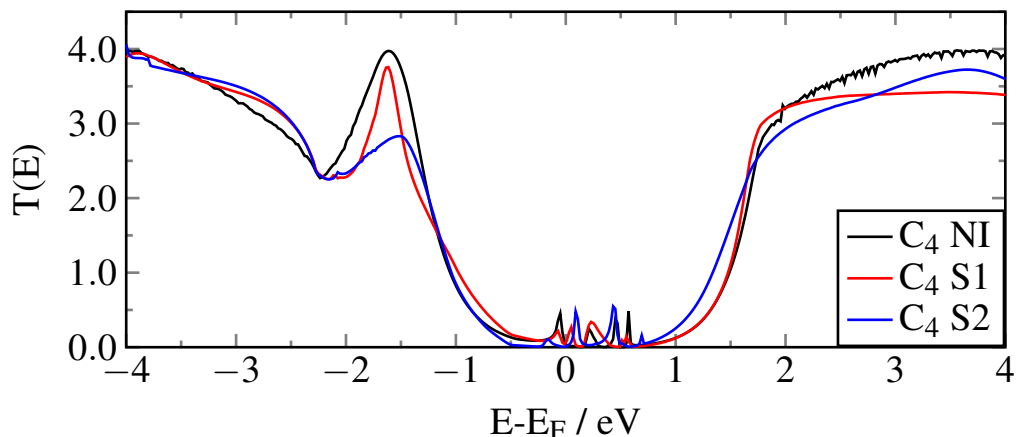
The transmission spectra of double C_8 chains are shown in fig 5.20 (third panel). C_8 1Z behaves similarly to C_4 1Z, showing two extra resonances at -0.21 and 0.9 eV in the transmission spectrum, both arising from the *LUMO* state, accompanied by self-doping ($\sim 0.4 |e|$) and a small charge transfer to the electrodes ($\sim 0.1 |e|$ per chain). However the approaching to the Fermi level and the reduction in magnitude of such extra resonances suggest that interference effects decrease with the chain length. For higher interchain distances any interference pattern turns out to be suppressed, with transmission spectra closely resembling the non-interacting chains one.

Non-parallel C_4 chains

We also considered the case of non-parallel C_4 chains in two different configurations, shown in fig. 5.22.

In the first structure one chain is placed obliquely and the other horizontally, determining a stretching of the first chain and a compression of the second, as is evident from the bond length analysis shown in fig. 5.22. In the second case both chains are placed obliquely and turn out to be characterized by triple bonds longer than those of horizontal C_4 chain, as a consequence of the junction geometry. Indeed the outermost carbons of the edge tend to preserve the sp^2 structure, forcing the chains to assume a zig-zag structure similar to that of a trans-polyacetylene.

The transmission spectra are only weakly affected by such geometrical modifications.

FIGURE 5.23: Transmission spectra of C_4 S1 and C_4 S2

In fact both geometries only show a small reduction of the broadening of the *HOMO* resonance, and C_4 S2 also a reduction in its magnitude. These results suggest that small changes in the chain geometry have marginal effects on the transport properties and that no interference effects occur.

Double C_4 R chains

We also investigated double C_4 R chains, in the geometries shown in fig. 5.19. C_4 R 1Z results highly unstable, since the atom of the edge in between of the chains should be hybridized sp^3 , and will not be considered for transport calculations. C_4 R 2Z shows a behavior similar to C_4 2Z (see fig. 5.20, bottom panel). Indeed, chain projected DOS analysis revealed that, as a consequence of the interchain coupling, the *HOMO* state splits, giving rises to two resonances at -1.34 and -0.91 eV (vs -1.34 eV of non-interacting chains). Contrarily, the *LUMO* state does not split but the corresponding resonance considerably narrows and shifts at higher energies, if compared with non-interacting case (1.09 eV vs 0.97 eV for the latter).

As opposite, the interchain coupling in C_4 R 3Z results in a splitting of the *LUMO* state, originating two resonances at 0.92 and 1.19 eV (vs 0.97 eV of non-interacting chains). A closer look at the chain PODS revealed that also the *HOMO* state is slightly split, featuring two peaks at -1.25 and -1.45 eV, although the corresponding resonances are not resolved. Thus, when compared with non-interacting case, the *HOMO* resonance only features a narrowing and a shift at higher energies (-1.18 eV vs -1.34 eV of non-interacting chains).

Similar is the behavior of C_4 R 4Z, featuring again a splitting of the *LUMO* state, resulting in two resonances at slightly lower energies (0.85 and 1.13 eV) while no splitting of

the *HOMO* has been found.

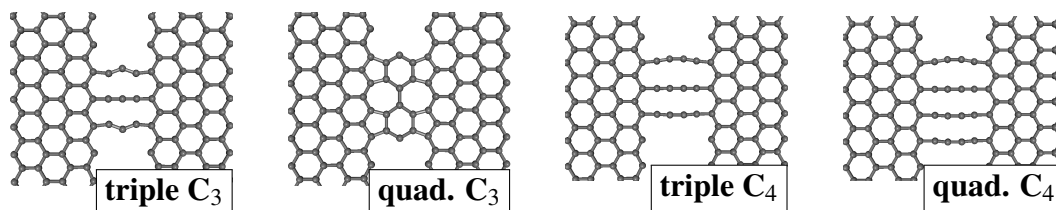
In conclusion we found qualitative different interference patterns depending on a number of issues, such as chain length, the interchain distance and the junction geometry. Specifically 1Z chains show destructive or constructive interference for odd and even chains, respectively. In the first case this arises from the distancing of the conductive states closer to the Fermi level, while in the latter from an additional broadening of the *HOMO* and *LUMO* states as a consequence of the interchain coupling. 2Z, 3Z and 4Z chains shows a different (constructive) interference pattern, originated by the splitting of the *HOMO* and/or *LUMO* states. We further noticed that the interference effects reduce as a function of both the interchain distance and the chain length.

Although the quantum origin of the interference in such systems is readily apparent, this has not resulted in effects analogous to those observed in mesoscopic systems (Aharonov-Bohm oscillations). Indeed, at the nanoscale, the conditions required for the observation of quantum interference have been described in terms of the spatial requirements on the wave function¹³⁹, and the interference acts in a subtle way, affecting the energy levels of the system. However, to date, neither a way to predict in what sort of structures these conditions might be observed nor a deep understanding of the phenomena giving rise to interference effects are clear.

Quantum interference has been predicted in related systems (cross-linking structures) by means of tight-binding models¹²⁸, in which interference effects in many cases dominate the spectrum. However, in general, such results turn out to be not in agreement with those suggested by density functional theory calculations. This mainly relates to the limits of the model, which does not allow features such as interchain coupling and junction geometry to be properly addressed, missing some aspects of the quantum behavior which turned out to be fundamental in describing interference patterns.

5.2.4 Multiple Chains

In this section we focus on the transport properties of systems in which more than two chains close to each other bridge the electrodes. In particular we investigated triple and quadruple C_3 and C_4 chains (see fig. 5.24) as well as a structure with an infinite number of C_4 chains.

FIGURE 5.24: Structures of triple and quadruple C_3 and C_4 chains

Multiple C_3 chains

As discussed in the previous sections, the transmission spectrum of single C_3 chain is characterized by two “*HOMO*” resonances close to the Fermi level, while C_3 1Z one shows an overall reduction of the magnitude of such resonances as a consequence of the distancing of the *HOMO* states from the Fermi level.

The behavior completely changes when triple chains are considered, whose transmission spectrum more resemble the single C_3 one, featuring the two “*HOMO*” resonances at about -0.4 and 0.8 eV (see fig. 5.25). As it is evident, such resonances are shifted by ~ 0.45 eV closer to the Fermi level and their magnitude (normalized with respect to the number of chains) is reduced by about 5 and 3 times, respectively, if compared with the corresponding resonance of single chain. This is a consequence of the partial disruption of the edge states, that causes a reduction of the coupling of the *HOMO* with the “conductive” bulk electrode states. The other resonances (*HOMO*₋₁ below -1 eV and *LUMO* above 1.5 eV) are not affected by this effect and only minor modifications result in the transmission spectrum.

In the quadruple chain structure, a significative structural distortion of the chains takes place, resulting in the formation of 5- and 7-atom rings along the edge. This effects is consistent with TEM experimental findings⁷⁰, in which narrowing of a graphene nanoribbon results in a structural reconstruction with formation of pentagonal and heptagonal rings. This strongly affects the transport properties, resulting in an overall reduction of the transmission, especially in the region [-0.5, 1.5] eV.

Multiple C_4 chains

Triple and quadruple C_4 chains show issues of the transport properties of both C_4 1Z and C_4 2Z, other than a general shift at lower energies of the whole transmission spectrum with the increasing of the number of chains. Specifically the triple chain features the two extra *LUMO* resonances at -0.68 and 1.0 eV (*vs* -0.39 and 1.25 eV for C_4 1Z), while for the quadruple chains they are slightly shifted downwards in energy (at -0.85 and 0.97 eV, respectively). In the latter case a further low-magnitude resonance still arising by

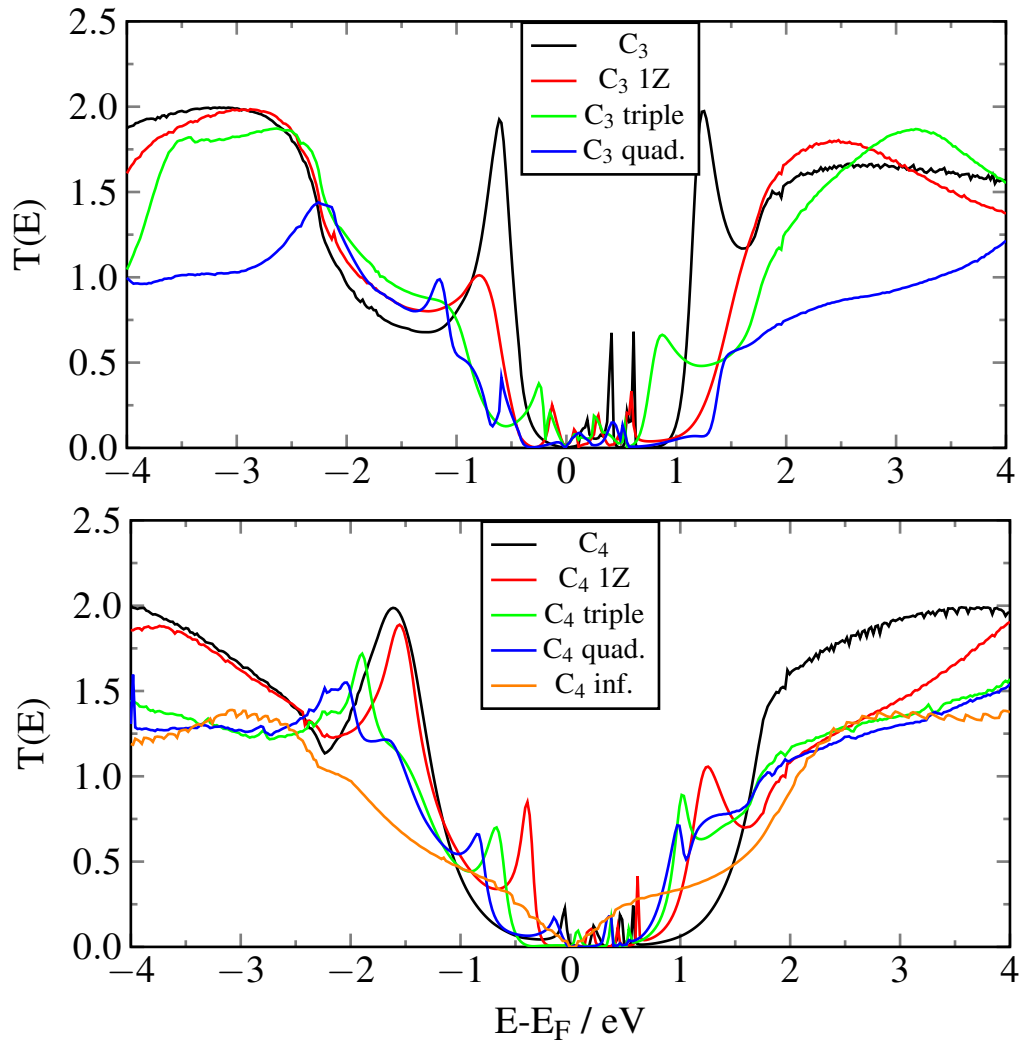


FIGURE 5.25: Transmission of multiple C_3 and C_4 chains. The transmission probabilities has been normalized with respect to the number of chains.

LUMO state appears at ~ 0.2 eV. However both the *HOMO* \rightarrow *LUMO* charge transfer ($\sim 0.5 |e|$) and the chain \rightarrow electrode charge transfer ($\sim 0.1 |e|$ per chain) are found to be irrespective of the number of chains. A closer look at the chain projected DOS further revealed a splitting of the *HOMO* state, although the corresponding resonances are not resolved and only a step-like peak appear at ~ -1.6 eV also because of the partial mixing with the *HOMO*₋₁ state.

Infinite number of C_4 chains

We further considered the case of an infinite number of C_4 chains bridging the graphene electrodes[‡]. We found a chain projected DOS characterized by a continuous of states,

[‡]This calculation was carried out by reducing the width of the cell in the x direction to one tenth with respect to that in fig. 5.3, in order to include only one chain in the simulation cell, while along the

as can be expected by extending the results for triple and quadruple chains to an higher number of chains. This reflects on the transmission spectrum, where no distinguishable resonances appear, and that turn out to be almost symmetric with respect to the Fermi level, where a very small gap is found (about 0.05 eV). From the Fermi level, the transmission increases by moving at higher or lower energies up to ± 2.5 eV, then becomes almost constant with an average value of 1.35. Notice that this value is much lower than the maximum theoretical value of 2 expected for a single chain and reached by the resonances of single C_4 chain. From the analysis of the LDOS we further found that the extremely high coupling among chains causes the *HOMO* and the *LUMO* states to span over all the negative and positive branches of the transmission spectrum, respectively, causing the *HOMO*₋₁ and the *LUMO*₊₁ resonances to be drifted outwards of the energy window reported in fig. 5.25.

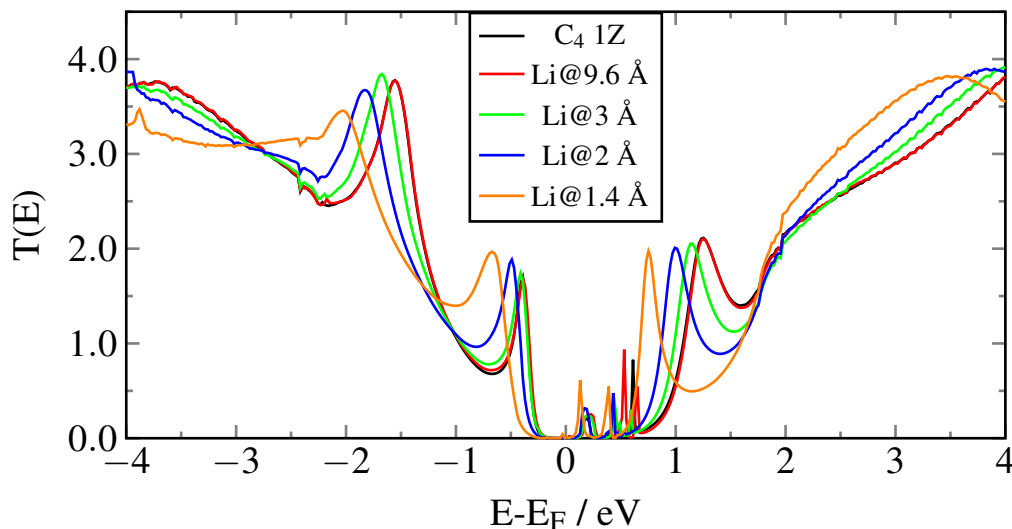
In this case it is difficult to determine whether interference effects occur or not, as well as quantify the self-doping charge transfer amount – although this effect is expected to occur, since contributions of *LUMO* state in the region [-0.5, 0] eV have been found – because the continuous of state in the chain projected DOS does not allow a proper integration of the projected DOS to this aim.

5.2.5 Li-induced gating

Recent advances in device fabrication have resulted in the developing of a number of methods for measuring two-terminal conduction through single or a small number of molecules, such as mechanical break junction, scanning probe approach (scanning tunneling microscopy, STM) or conducting probe atomic force microscopy. The extension of such methods to three-terminal devices has been extremely challenging because of geometrical and electrostatic constrains. In fact, the third terminal should be only capacitively coupled to the molecule, modulating the charge carrier population of the channel without inducing any structural modifications.

Clearly it is unreasonable to expect such devices to act like standard MOSFETs (metal oxide semiconductor field effect transistors), but rather they operate more like single-electron transistors, with transport mainly dominated by Coulomb blockade. These devices act as switches, allowing the current to flow only when the molecular states lie within the electrochemical potentials of source and drain leads. This tuning is achieved

other directions the dimensions are unchanged. In order to achieve a k-space sampling as in the other calculations, a k-mesh of 30×1 and 200×1 has been used in optimization and transport calculations, respectively

FIGURE 5.26: Li-induced gating effects on C₄ 1Z structure

by varying the gate voltage. Application of a positive voltage shifts downwards in energy the electrochemical potential of the molecule (*i.e.* the molecule is reduced), thus the energy levels, whereas a negative voltage shift up the electrochemical potential resulting in the oxidation of the molecule.

One way to realize in practice three-terminal devices is the so-called chemical gating, *i.e.* to use electron-attractors or donators atoms to induce an electrostatic field acting as a gate potential, achieving an *in situ* gate-controlled charge transport.

Here, in particular, we investigate the effects of gating induced by a lithium atom on the transport properties of double C₄ (1,2) chains, chosen as a benchmark for all geometries investigated in the previous sections.

For such calculation we positioned the lithium atom in the electrode plane alongside of a chain at different distances (1.4, 2, 3 and 9.6 Å), assuming negligible effects on the geometry. In particular the shortest distance (1.4 Å) corresponds to C-Li bond lengths of ~ 2 Å, consistent with typical lengths in organolithium compounds¹⁴⁰, while the largest (9.6 Å) to half simulation cell.

As expected, a significative charge transfer from the lithium to the chain and the electrodes occurs, depending on the chain-Li distance. For the largest distance $\sim 0.5 |e|$ are transferred from the Li to the electrodes, while chains do not gain charges. Surprisingly, such charge transfer does not induce significative modifications in the transmission spectrum of C₄ 1Z (see fig. 5.26) probably because the symmetry of the system is preserved.

When the Li approaches the chains the charge transfer increases, with ~ 0.15 (0.25) $|e|$ transferred from the Li to the closest atoms of the chains and ~ 0.4 (0.35) $|e|$ transferred

to the electrodes for a Li-chain distance of 3 (2) Å. For the shortest distance, corresponding to the formation of a Li-C ionic bond, a further increasing of the Li-chain charge transfer has been found ($\sim 0.6 |e|$) accompanied by a reduction of the charge transferred to the electrodes ($\sim 0.2 |e|$). As expected, this results in a progressive shift downwards in energy of the electronic states of the system, and in turn of the resonances of the transmission spectrum, with only minor modifications induced by the symmetry breaking, indicating that the Li mainly act as a capacitively coupled gate. In particular, notice that the two interference resonances slightly approach to each other with the increasing of the Li-chain charge transfer because the interference resonance above the Fermi level is highly affected by the gating effect.

5.2.6 Molecular switches

Molecular switches are the basic elements of control in any electronic architecture at the nanoscale, since they either allow current to flow or not. In practice a molecular switch works in the same way as the “macroscopic” switches used every day to turn electronic appliances on and off. Hence, the creation of functional molecular devices able to change their structural, electronic or optical properties in response to external stimuli turns out to be the ultimate limit of scaling of integrate circuits. Thus, molecules that, depending on the environmental influences, can switch among different stable states separated by an activation barrier much larger than the thermal energy $K_b T$, are promising candidates for such application.

A variety of external stimuli such as light, electric field, temperature, tunneling electrons and even chemical or mechanical modifications can be used to activate the molecular switches by manipulating molecular conformations, dipole orientations, spin states, charge states or chemical bond formation.

There are many examples of proposed molecular and atomic switches, which use a myriad of different mechanisms and motifs for operation. Aside from simple switches¹⁴¹, there have also been several suggestions of more complex switching behaviors, which involves the use of two-terminal resonant tunneling¹⁴² or the use of arrays of switches to implement logic operations^{143,144}. Moreover a number of molecular switching based on quantum effects such as quantum interference and phase decoherence have been suggested^{128,145}.

Here, we explore a class of conductive molecules that can be driven between high- and low-conductive states by mechanical forces.

In particular, we discuss in details the case of a benzenic ring contacted with the zigzag

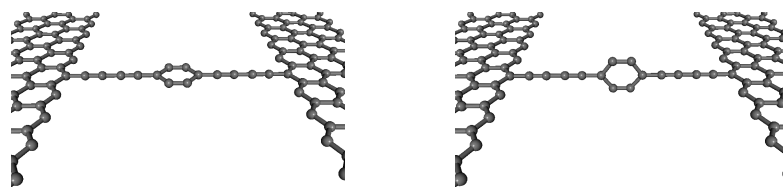


FIGURE 5.27: Structures of planar (left) and orthogonal (right) C_4 -benzene- C_4

graphene electrodes through C_3 and C_4 carbon chains, for which, in principle, the current can be switched on and off by simple rotation of the molecule. In fact we expect that the conduction process takes place only in a planar geometry, in which the π_{\perp} molecular orbitals of the chain-benzene-chain molecule overlap with the π electron cloud of graphene. This condition no longer holds when benzene is mechanically rotated by 90° . These results will be useful as starting point to investigate more complex systems, *e.g.* in which an electrode is rotated with respect to the other or in which benzene is replaced, for instance, by a polyaromatic structure. In particular we will briefly address the case of a coronene connected to graphene edges through C_3 and C_4 chains.

In principle such devices can be produced experimentally by carbon sputtering of graphene sheets. However their implementation under lab conditions and in particular the control of the rotation of the molecule still faces several challenges which could be worth considering in the coming years. Although we consider very simple devices, a suitable molecular switch could be the basis for more complicated molecular machines with applications in nanotechnology, biomedicine and computational chip design.

The study presented in this section has been carried out by analyzing the evolution of the transmission function and the density of states as a function of the angle of rotation (θ) of benzene (coronene) as well as comparing the molecular level coupled with the electrodes with the molecular orbitals of the hydrogen-terminated gas-phase molecule. The latter have been calculated by means of DFT/PBE method as implemented in the GAMESS code expanding the wavefunction in a SZ(+P) basis-set and using the geometry of the contacted molecule.

C_4 -benzene- C_4

We first analyzed in details the transport properties of a benzene connected to the electrodes through C_4 chains. The planar and the orthogonal configurations of the molecule are shown in fig. 5.27. Despite the free rotation of the benzenic ring under ambient conditions can be expected, we found a significative rotational barrier between the planar and orthogonal geometries, the first being more stable by 0.48 eV. This is a consequence

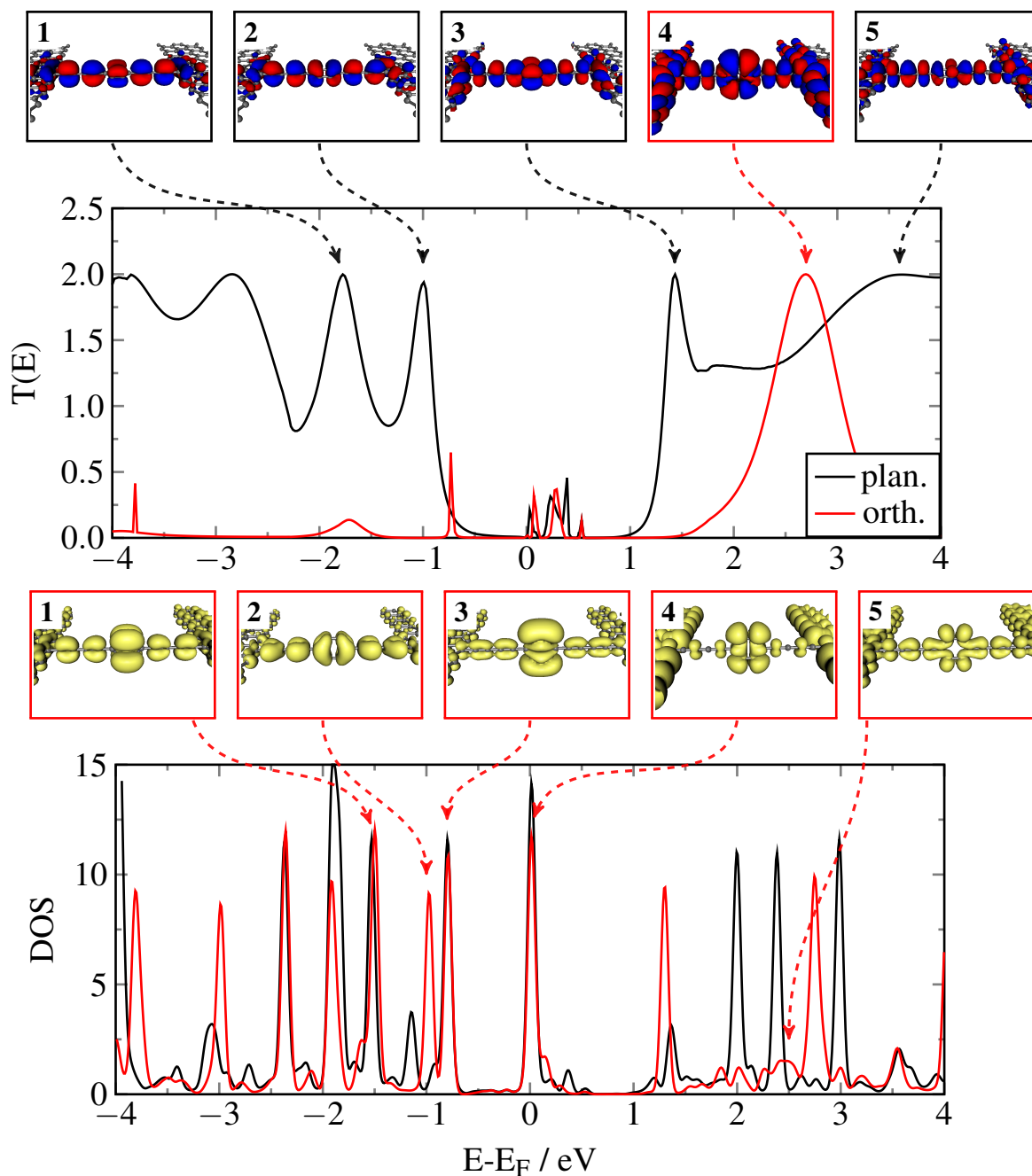


FIGURE 5.28: Top: transmission and eigenchannels of C_4 -benzene- C_4 . Bottom: chain projected DOS and LDOS pictures. Data related to orthogonal (planar) benzene are shown in red (black). See text for details.

of the partial polyene-cumulene hybridization of the chain, featuring a chain-benzene bond with length of 1.42 \AA , intermediate between simple and double bond length of typical hydrocarbons and comparable with the $C - C$ bond lengths in the benzenic ring (1.41 \AA) that hinders the free rotation of the ring.

In fig. 5.28 we reported the transmission and the chain projected DOS for such system. The identification of the level of the chain-benzene-chain molecule giving rise to the

resonances in the transmission spectrum is performed by comparing the eigenchannels with both the local density of states (LDOS) and the molecular orbitals of the hydrogen-terminated gas-phase molecule. These results are summarized in fig. 5.29.

The chain projected DOS in the planar configuration ($\theta=0^\circ$) is characterized by a number of sharp peaks, due to non-conductive states, that being only weakly hybridized with the electrodes, remain localized in energy. In particular the *LUMO*, the *HOMO*₋₆ and *HOMO*₋₅ are not conductive since they are mainly localized on the benzene. For the first and the second the main contributions to the electronic state arise from the p_{\parallel} [§] atomic orbitals of the ring and from the *s* orbitals of the chain, while only the p_{\perp} of benzene contributes to the latter. These states are localized at the Fermi level, at ~ -2.37 eV and ~ -1.53 eV, respectively.

Other state are not conductive since are localized only on the chains, such as the *HOMO*₋₃ and the *LUMO*₊₃, in which only the *s* atomic orbitals of the ring atoms and the p_{\parallel} of the chain atoms have a significative contribution.

Others are not conductive, although they extend on the whole molecule, as a consequence of the negligible overlap with the π electron clouds of the electrodes. This is the case of the *HOMO*₋₁, the *LUMO*₊₂ or the *LUMO*₊₄.

The remaining states turn out to be conductive in the planar geometry, and generate the resonances in the transmission spectrum. In particular the *HOMO*₋₇, the *HOMO*₋₄, the *HOMO* and the *LUMO*₊₁ give rise to the resonances at about -2.7, -2.15, -1.1 and 1.2 eV, respectively. This is also confirmed by eigenchannels analysis (see fig. 5.28, eigench. 1, 2, 3 and 5). The wide resonance above 1.7 eV arises by the mixing of the *LUMO*₊₅ and the *LUMO*₊₇ (not shown).

In the orthogonal configuration ($\theta=90^\circ$), the projected DOS features an higher number of sharp peaks with respect to the planar case, since the electronic states conductive in the planar geometry are no longer strongly coupled with the electrode and turn out to be localized in energy. This results in a dramatic lowering of the transmission probabilities at all energies, except for a large resonance at about 2.6 eV, arising from the *LUMO*₊₂ state. Indeed this is a peculiar state in which the p_{\parallel} atomic orbitals of both chains and ring have the largest contribution. In the planar geometry, it forms a sharp peak in the DOS at 2 eV while for $\theta=90^\circ$ it spans over the energy range [1.5, 3.8] eV as a consequence of the increased coupling with the electrodes. The LDOS in the energy region [2.3, 2.6] eV is reported in fig. 5.28 (ldos n. 5). In the same figure, the LDOS of four non-conductive states in the orthogonal geometry are also shown (ldos n. 1-4). The first and the second states are not conductive because of the negligible chain-benzene

[§]Here we adopt the same notation described in sect. 5.2.1

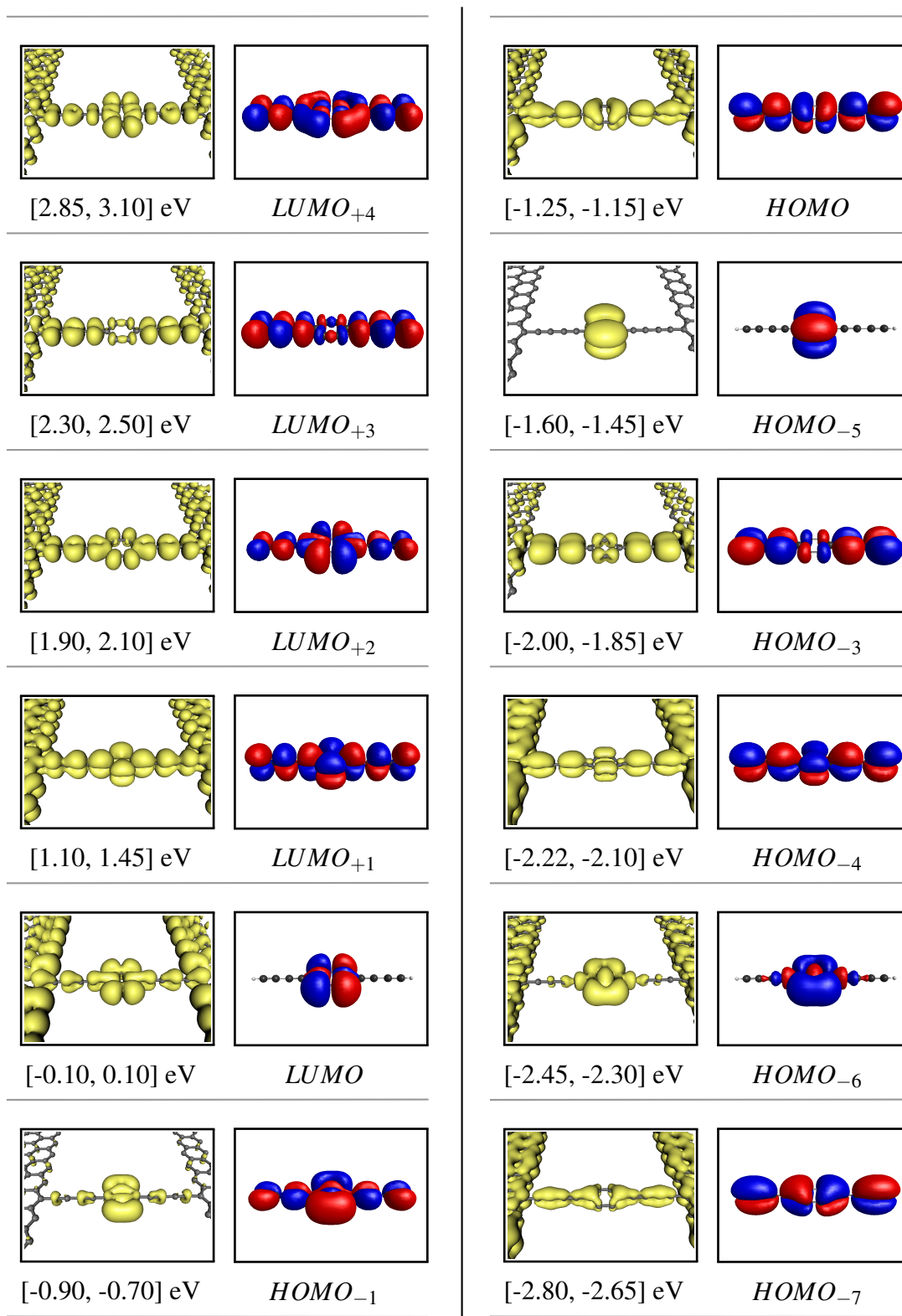


FIGURE 5.29: LDOS of C_4 -benzene- C_4 and corresponding molecular orbitals of the hydrogen-terminated gas-phase molecule. The integration range of the DOS is reported between square brackets.

and chain-electrode overlap, respectively. The third (the $HOMO_{-1}$), in principle, could conduct, but this state is strongly localized in the DOS for both the planar and the orthogonal configuration, suggesting that it weakly couples with the electrodes in both cases, giving rise only to the weak resonance at -0.7 eV. The latter is not conductive since it is mainly localized to the benzenic ring only.

The transmission spectra as a function of θ are shown in fig. 5.32. Upon rotation of 15° , no significant changes in the transmission of the occupied states occur, while the transmission of the $LUMO_{+1}$ drastically decrease in the region [2.0, 2.5] eV and the resonance of the $LUMO_{+2}$ already appears at about 2.05 eV. Further rotations cause a fast reduction of the width of the $HOMO_{-4}$, the $HOMO$ and the $LUMO_{+1}$ resonances, that reduce to sharp peaks for $\theta=75^\circ$ and almost disappear for $\theta=90^\circ$. This reduction is slightly slower for the $HOMO_{-7}$, the $LUMO_{+5}$ and the $LUMO_{+7}$. The $HOMO_{-2}$ resonance progressively shifts at higher energies (from 2.05 eV for $\theta=15^\circ$ to 2.6 eV for $\theta=90^\circ$) and spreads in energy as a consequence of the progressive coupling with the π electron cloud of graphene.

The resonance of the $HOMO_{-1}$ state appears at $\theta=15^\circ$, its magnitude progressively increases reaching a maximum of about 1.7 for $\theta=45^\circ$, then decreases to about 0.7 for $\theta=90^\circ$.

C₃-benzene-C₃

As opposed to the previous case, the orthogonal geometry results 0.76 eV more stable than the planar one, as a consequence of the cumulenenic behavior of odd chains, resulting in a chain-benzene bond length of 1.38 Å.

The transmission and the chain projected DOS are reported in fig. 5.30. As in the previous case, a comparison between eigenchannels, LDOS and molecular orbitals of the isolated molecule is helpful in understanding the electronic structure of the device and its behavior upon rotation of the benzene. These results are summarized, for the planar configuration, in fig. 5.31.

The conductive states can be easily identified. The large resonance below -2.5 eV arises from the $HOMO_{-6}$ (not shown), the resonances at about -2.0 and -0.9 eV from the $HOMO_{-4}$ and the $HOMO_{-1}$, respectively. Those above the Fermi level are generated by the $LUMO_{+2}$ (at about 1.45 eV) and the $LUMO_{+4}$ (above 1.7 eV).

The $HOMO$ orbital results mainly localized on the benzene, thus it weakly interacts with the electrodes and is not conductive both in the planar and in the orthogonal configuration, resulting in a sharp peak in the DOS at the Fermi level in both cases.

Different is the behavior of the $LUMO$. The $LUMO$ of the gas-phase molecule is mainly

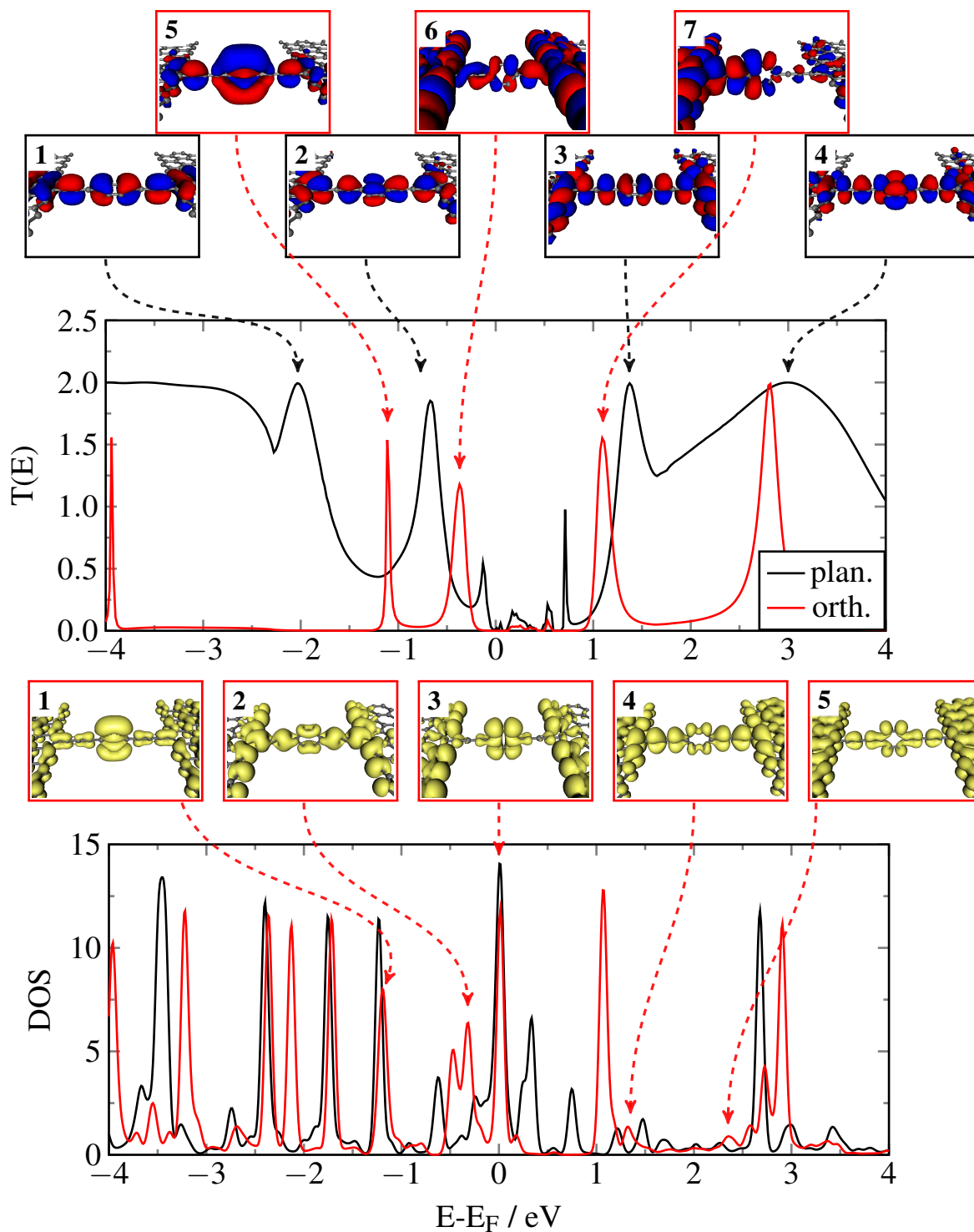


FIGURE 5.30: Top: transmission and eigenchannels of C_3 -benzene- C_3 . Bottom: chain projected DOS and LDOS pictures. Data related to orthogonal (planar) benzene are shown in red (black). See text for details.

localized on the chains, but also have an important contribution from the $p_{||}$ atomic orbitals of the ring. When the molecule is contacted with the electrode, the *LUMO* become stabilized and drop below the *HOMO*. Although it is not conductive in the

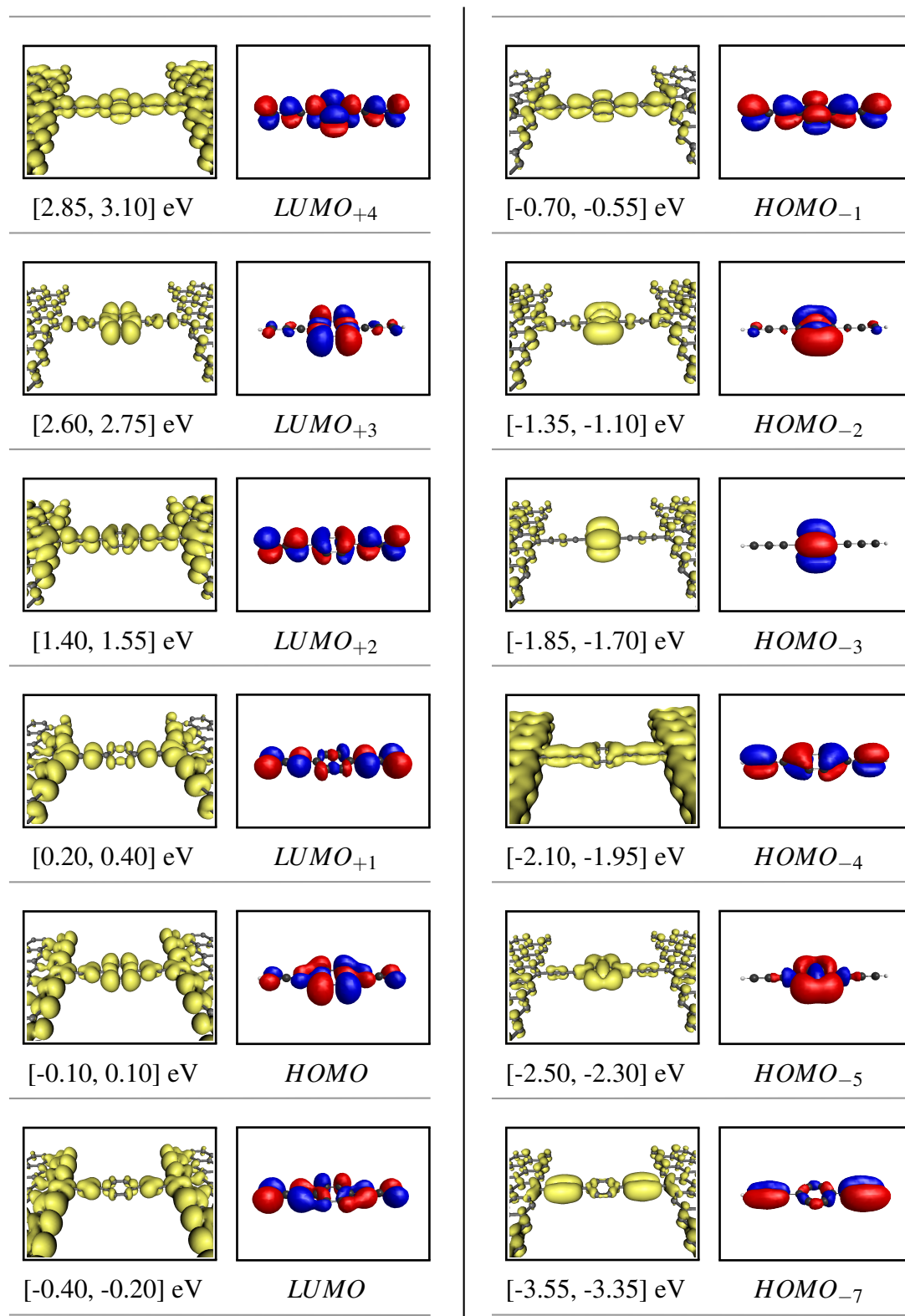


FIGURE 5.31: LDOS of C_3 -benzene- C_3 and corresponding molecular orbitals of the hydrogen-terminated gas-phase molecule. The integration range of the DOS is reported between square brackets.

planar geometry, it possesses the requirements to become conductive in the orthogonal geometry, giving rise, in fact, to the sharp resonance at about -0.45 eV. Notice that in the orthogonal configuration, it lies in the same energies range as the non-conductive $HOMO_{-1}$, thus the LDOS results in a mixing of the two. In this case the eigenchannels, showing only the conductive state, are more helpful for its identification. (see fig. 5.30, eigench. n. 6 and LDOS n. 2).

The $LUMO_{+1}$ features characteristics and a behavior similar to the $LUMO$. It is not conductive in the planar geometry since it lies in the electrode plane and form the narrow peak at about 0.3 eV in the projected DOS. Upon rotation of the benzene it shifts at higher energies, originating the resonance at about 1.1 eV.

Completely different is the case of the resonances at about -1.2 eV and 2.35 eV in the spectrum of orthogonal graphene. These arise from the $HOMO_{-2}$ and from the $LUMO_{+3}$, respectively. As a consequence of the small contribution of the $p_{||}$ atomic orbitals of the chain atoms (however higher than the other orbitals), these states are mainly localized on the benzenic ring both in the gas-phase molecule and in the planar geometry. As opposite, in the orthogonal geometry, they result delocalized on the whole molecule as a consequence of the increased chain-electrode coupling, becoming conductive.

The transmission spectra as a function of θ are shown in fig. 5.32. As in the C_4 case, the transmission of the state highly spread in energy reduces first. Upon rotation of 15° two discontinuities in the transmission appear at -3.5 and 2.7 eV, indicating that the $HOMO_{-6}$ and the $LUMO_{+4}$ start to decouple from the electrodes. Further rotations cause the transmission of such states to rapidly decrease, completely nullifying for $\theta=75^\circ$. Otherwise, the width of the resonances of $HOMO_{-4}$, $HOMO_{-1}$ and $LUMO_{+2}$ progressively reduces with the rotation, but sharp resonances are still visible for $\theta=75^\circ$, vanishing only for $\theta=90^\circ$.

While the $HOMO_{-2}$ appears for $\theta=15^\circ$ at -1.17 eV and slightly shifts at higher energies upon rotation (up to -1.0 eV for $\theta=90^\circ$), the $LUMO_{+3}$ only appears for $\theta=60^\circ$ at 0.73 eV, then shifts to 0.93 eV for $\theta=75^\circ$ and finally to 1.1 eV for $\theta=90^\circ$.

In conclusion, for benzene contacted with electrodes through carbon chains, a non-conductive state in the planar geometry becomes conductive upon rotation by 90° only if it extends over the whole molecule and it has almost a small contribution of $p_{||}$ atomic orbitals of all atoms. The higher this contribution, the stronger the coupling with the electrodes and the wider the resonances. Thus, a simple knowledge of the molecular orbitals is helpful in a first estimation of the transport properties in the planar and

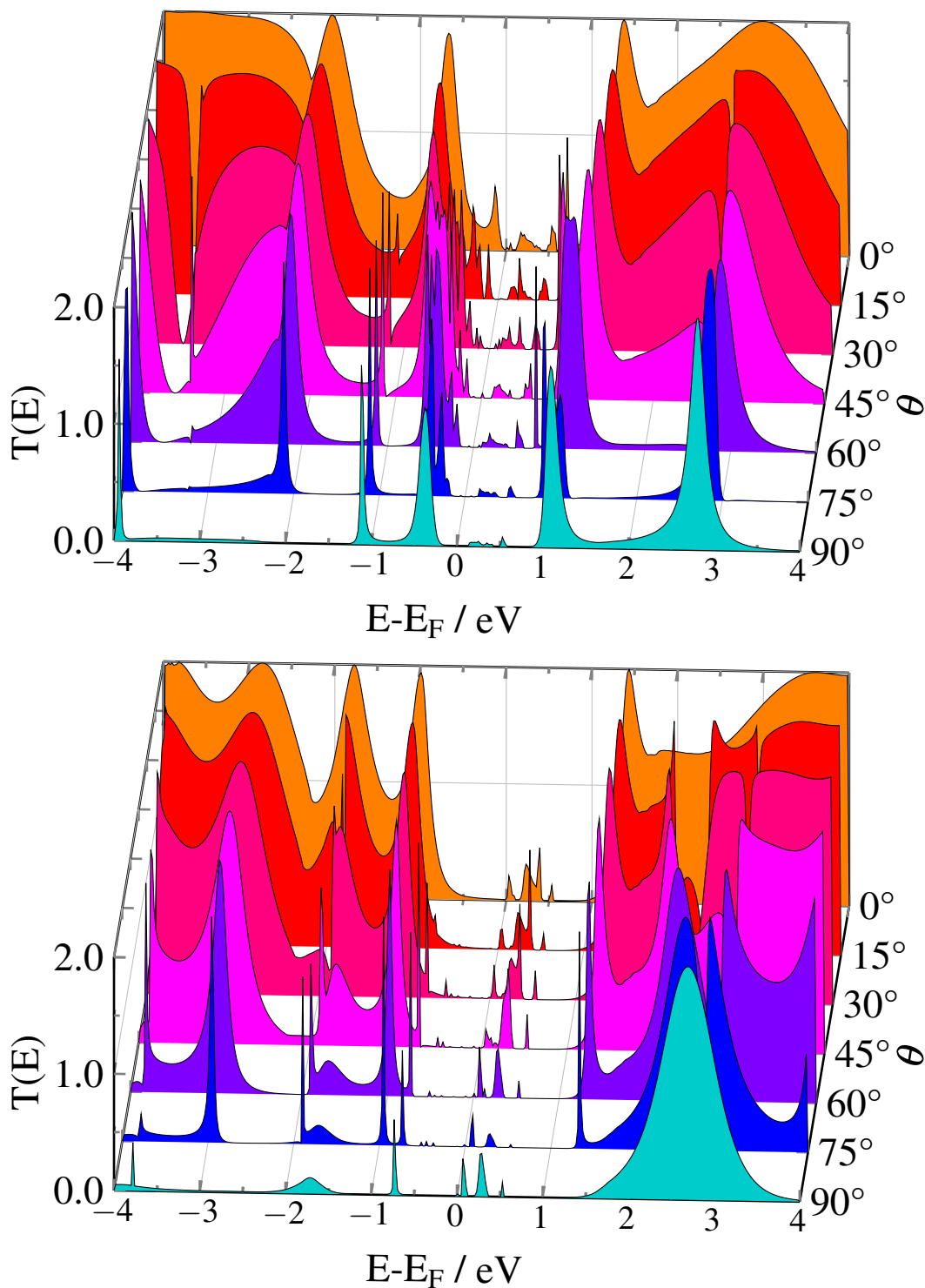


FIGURE 5.32: Transmission of C_3 -benzene- C_3 (top) and C_4 -benzene- C_4 (bottom) molecules as a function of the angle between the benzene and the electrodes

orthogonal configurations, allowing to gather informations about the number of conductive channels. Of course nothing can be said about their position in the transmission spectrum, since the coupling with the electrodes deeply modify their energy.

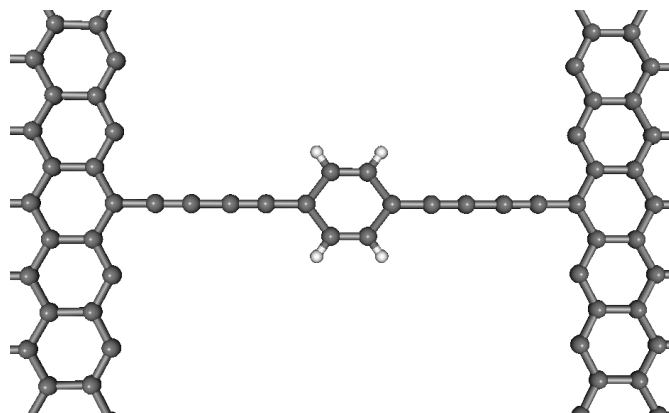
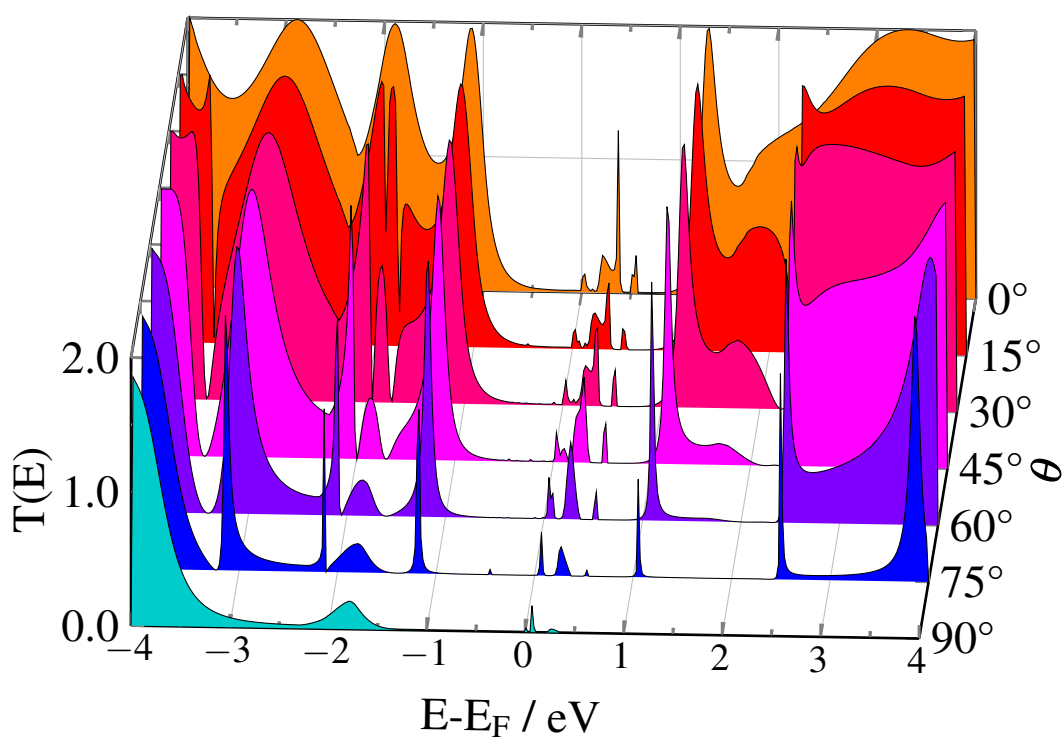
The results also strongly depend on the number of carbon atoms of the chains. In fact, reflecting the results of single carbon chains, we expect an odd-even oscillating behavior concerning both the low-transmission window across the Fermi level region (larger for even chains) and the number of conductive states in the orthogonal geometry (higher for odd chains).

$C_4-C_6H_4-C_4$

So far we have considered structures containing only C-C bonds, since in the typical experimental setup, dangling bonds result on the outermost edge-carbon atoms as well as in the benzenic ring. Here we will show that the binding of hydrogen atoms on the dangling bonds of benzene (see fig. 5.33) strongly affects the transport properties in the orthogonal C_4 -benzene- C_4 geometry, since the $p_{//}$ atomic orbitals of benzene are no longer available for the conduction.

The results are shown in fig. 5.34. The comparison with fig. 5.32 features no significative changes in the transmission of the planar geometry (except for a small shift of about 0.08 eV downwards in energy of the whole spectrum, probably related to a small charge transfer from the hydrogens to the chain) since the π_{\perp} states of the molecule are unaffected by the presence of the hydrogens.

Upon rotation of 15° , some states start breaking down, and, for further rotations, a general narrowing of the resonances occurs. At $\theta=75^\circ$ the transmission spectrum features only few resonances, mostly arising by conductive states in the planar geometry, such as the $HOMO_{-7}$ at -3.14 eV, the $HOMO_{-4}$ at -2.135 eV or the $LUMO_{+1}$ at 1.05 eV. The only exceptions are the resonances at 2.5 eV, arising from the $LUMO_{+2}$, *i. e.* the only conductive state in the orthogonal geometry without hydrogens, and the one at -4 eV. This, in particular, as a function of θ , shows a decreasing contribution from a conductive state in the planar geometry, and an increasing contribution by a $\pi_{//}$ state, conductive in the orthogonal geometry, thus resulting in a constant magnitude. However, this is not interestingly for practical applications, since its inclusion in between of the source and drain electrochemical potentials would require a bias of almost 8 V. Upon further rotation of 15° , all these resonances disappear, except the latter and a low-magnitude resonance at about -1.8 eV deriving from $HOMO_{-4}$ state. Finally, in the orthogonal geometry, the conduction is switched off for a large energy range, providing a device with an on/off current ratio close to 100% and low leakage current.

FIGURE 5.33: Structure of C₄-C₆H₄-C₄FIGURE 5.34: Transmission of C₄-C₆H₄-C₄ molecule as a function of the angle between the benzene and the electrodes

C_n-coronene-C_n

We also briefly investigated the case of a coronene contacted to graphene electrodes through C₃ and C₄ chains. The transmission as a function of rotational angle is shown in fig. 5.36. A comparison between the eigenchannels of some of the resonances and the molecular orbitals of the hydrogen-terminated gas-phase molecule is shown in fig. 5.35.

For both chains, the transmission spectrum of the planar geometry shows a large number of sharp and well-separated resonances. This is mainly due to (i) the higher number of

states in the energy range considered with respect to the benzene case, (ii) the weak coupling with the electrodes for a large number of conductive molecular states, which turn out to be mainly localized on the coronene and (iii) the high number of non-conductive states, giving rise to several energy windows where the transmission is close to zero, especially in the C_3 case.

As for benzene molecule, the region around the Fermi level is characterized only by weak resonances, since the *HOMO* and the *LUMO* states turn out to be not conductive. This poorly conductive region is more extended for the C_4 -coronene- C_4 (from -0.4 to 1.2 eV), except for some weak resonances arising from the $LUMO_{+1}$, than for C_3 -coronene- C_3 (from -0.2 to 0.8 eV), reflecting the behavior of single chains.

In the C_3 case the resonances closer to the Fermi level correspond to the $HOMO_{-3}$ and to the $LUMO_{+7}$ (shown in fig. 5.35). While *HOMO*, *LUMO* and $LUMO_{+1}$ are never conductive (the first and the second are localized only on half molecule, the latter has contributions arising from p_{\perp} atomic orbital of one chain and p_{\parallel} atomic orbitals of the other chain), the states from $LUMO_{+3}$ to $LUMO_{+6}$ become conductive in the orthogonal configuration, giving rise to the resonances in the region [0.8, 2.0] eV[¶]. All these states are characterized by a significative contribution of p_{\parallel} orbitals of all atoms of the molecule, but higher for coronene atoms. This results in a molecular state mainly localized on the coronene, thus not strongly couple with the electrodes, explaining the sharp resonances appearing in the transmission spectrum. The same holds for the resonance at -2.04 eV, arising from the $HOMO_{-7}$.

In the C_4 -coronene- C_4 the resonances closer to the Fermi level arise from the $HOMO_{-1}$ (from -0.7 to 0.6 eV) and from the $LUMO_{+3}$ (at 1.53 eV). As in the corresponding benzene case, upon rotation by 90° , few resonances appear in the transmission spectrum, these arising from the $HOMO_{-9}$ (at -1.82 eV) and the $HOMO_{-7}$ (at -1.37 eV) providing the highest magnitudes. The $LUMO_{+2}$ and the $LUMO_{+4}$ are mainly localized on the coronene and generate the very weak resonances at 1.53 and 1.79 eV respectively. In general, these results reflect the behavior observed for C_n -benzene- C_n structures, confirming their extensibility to more complex polyaromatic molecules.

[¶]Specifically the resonance at 0.93 eV is due to the $LUMO_{+3}$, the one at 1.13 eV to both the $LUMO_{+3}$ and the $LUMO_{+4}$, those at 1.31, 1.53 and 1.87 eV arise from $LUMO_{+4}$, $LUMO_{+5}$ and $LUMO_{+6}$, respectively

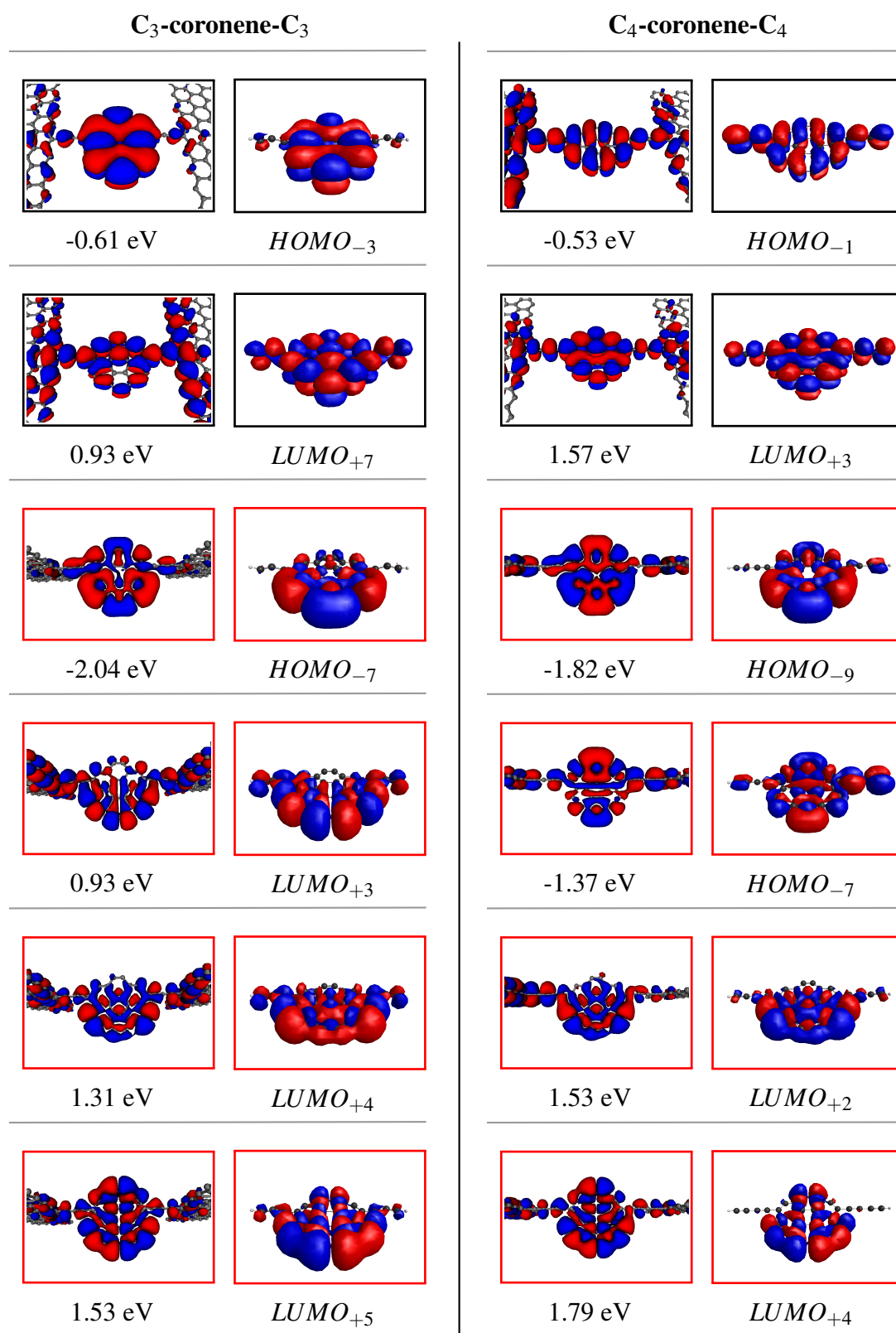


FIGURE 5.35: Comparison between the eigenchannels of C_3 -coronene- C_3 (left) and C_4 -coronene- C_4 (right) and the corresponding molecular orbitals of the gas-phase molecule. Black (red) boxes refer to the planar (orthogonal) configuration.

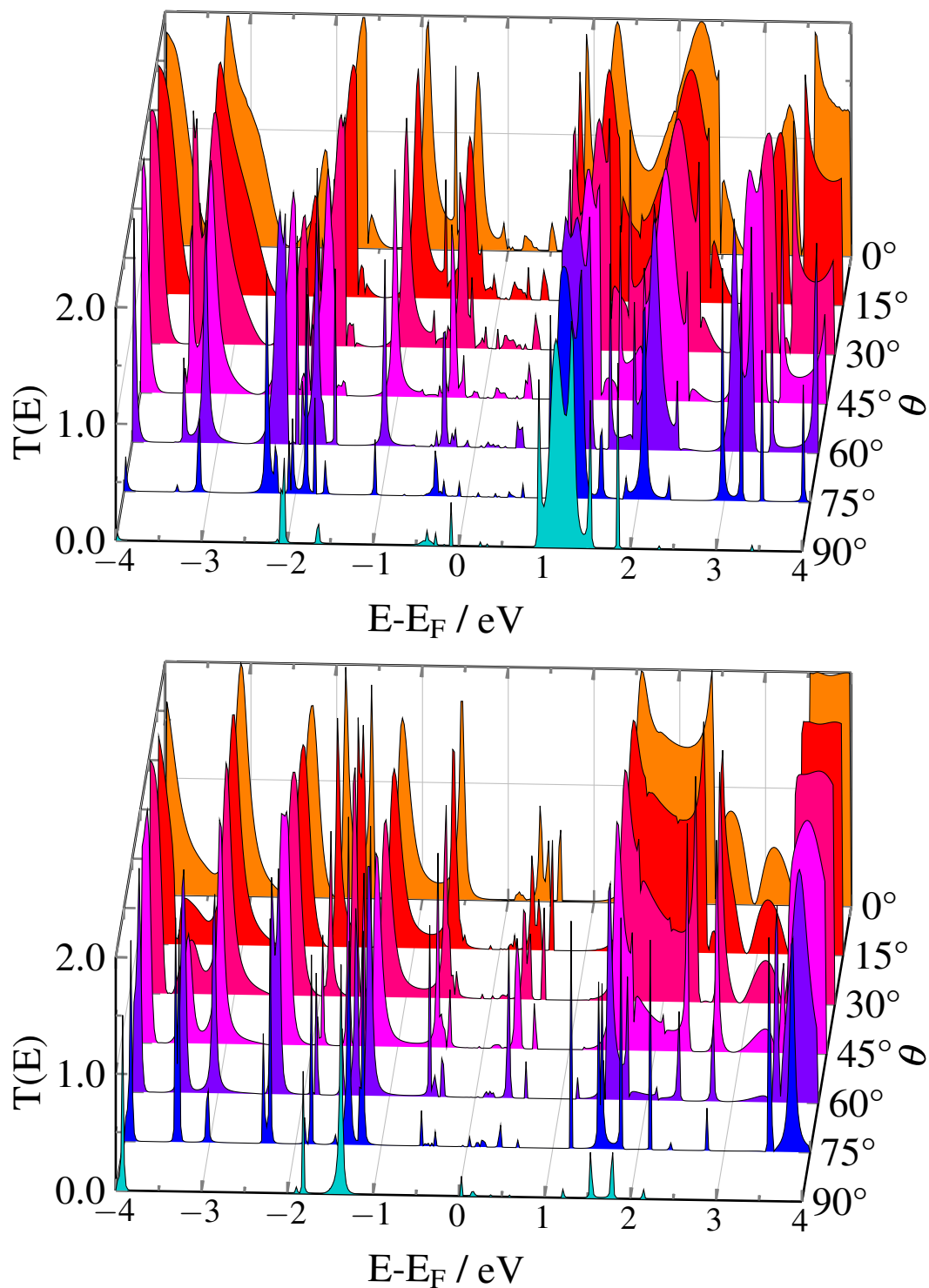


FIGURE 5.36: Transmission of C₃-coronene-C₃ (top) and C₄-coronene-C₄ (bottom) molecules as a function of the angle between the coronene and the electrodes

5.3 Armchair electrodes

In this section we discuss in details the transport properties of single chains contacted with armchair edge-shaped nanoribbons. In particular we investigated the three different geometries allowed by this edge configuration, either forming a single chain-electrode bond (C_n) or a three- or five-atom ring at the junction (C_n 3R and 5R, respectively), as shown in fig. 5.37.

As expected, the geometry of the junction strongly affects the structural characteristics of the chain. Noteworthy, we found close similarities with the behavior of zigzag-bound chains. First, odd chains turns out to be cumulenic for all junction configurations, while even chains features a prevalent polyynic character. Second, the chains forming a ring at the junction show an inversion of the BLA, suggesting a radicalic character, with unpaired electrons mainly located on the terminal atoms. However, C_n armchair-bound chains are characterized by a more marked cumulenic behavior with respect to the zigzag-bound ones. For instance, C_7 and C_8 chains connected with the armchair

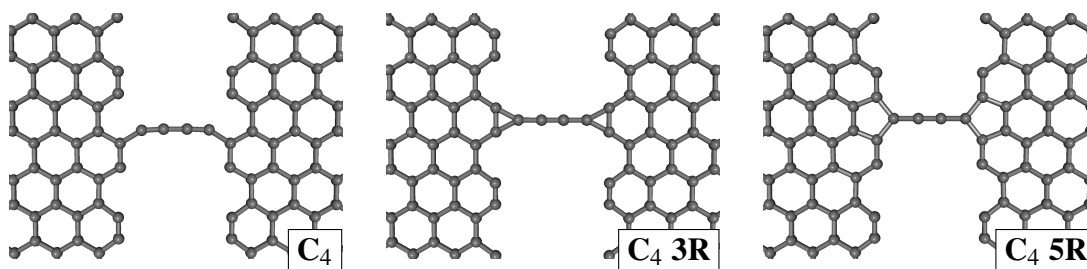


FIGURE 5.37: Structures of single C_4 chains contacted with armchair electrodes

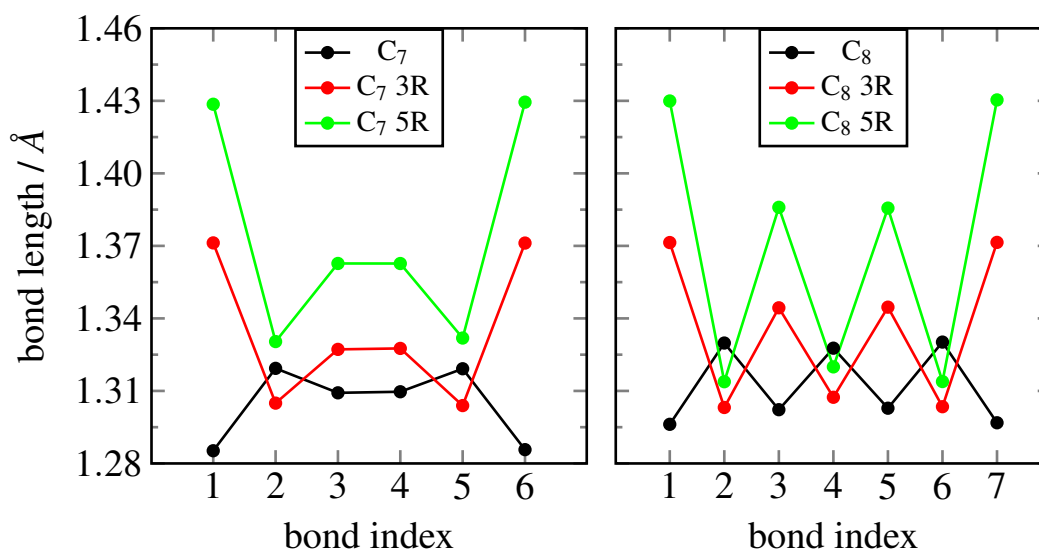


FIGURE 5.38: Bond lengths of C_7 and C_8 connected to armchair electrodes

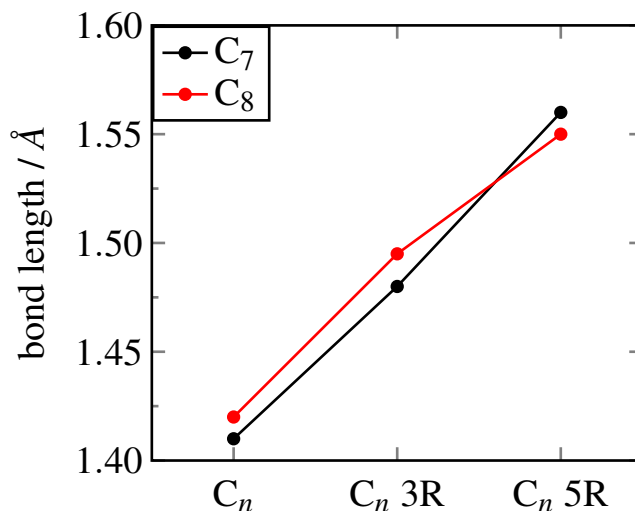


FIGURE 5.39: Chain-electrode bond lengths for the structures described in the text

edge feature BLA values in average ~ 1.5 and ~ 3 times lower than in the zigzag case, respectively.

A closer look at the bond lengths of C₇ (fig. 5.38) revealed a perfect cumulenic character in the middle of the chain and a significant increasing of the BLA toward the terminations, particularly evident for the 3R and 5R structures. Moreover, C₇ 5R shows a significant stretching of the chain induced by the strain of the pentagonal ring at the junction, resulting in bonds 0.3-0.6 Å longer than the 3R. Similar results hold for C₈, the 5R chain featuring the more marked polyynic character.

Such results are strictly related to the chain-electrode bond lengths, reported in fig. 5.39, that turn out to be almost independent on the chain length. For C_n we found values comparable to that of the zigzag-bound chains (1.38 (1.42) vs 1.41 (1.42) Å for C₇ (C₈)), while bonds considerably longer result for the 3R (~ 1.49 Å) and 5R (~ 1.56 Å) geometries.

These characteristics are reflected on the density of states and, in turn, on the transport properties. As for zigzag nanoribbons, we first performed electronic structure calculations on the same cell used in transport calculations (fig. 5.3) in order to compute the DOS of the system. We point out again that such calculations refer to a physical system different from that considered in transport calculations (periodic vs semi-infinite), however, if the nanoribbon is large enough, many issues also hold for the semi-infinite system.

The armchair nanoribbon (27-AGNR using the conventional nomenclature) itself turns out to be metallic and characterized by antiferromagnetic order. In the energy range considered, the π_{\perp} states dominate the DOS. However, the Fermi level region (from

-0.4 to 0.5 eV) is characterized by a small number of π_{\perp} states, slowly increasing distancing from the Fermi level up to -1.8 and 1.5 eV, where a significant increment of π_{\perp} states occur (see fig. 5.40). Moreover, the integration of the DOS also revealed a significant charge transfer ($\sim 0.074 |e|/\text{atom}$) from the π_{\perp} to the σ states of bulk atoms (depicted as electrodes in fig. 5.3) and a small charge transfer ($\sim 0.015 |e|/\text{atom}$) from π_{\perp} bulk to π_{\perp} edge states.

Next we considered the effects of the binding of a C_7 chain on the DOS. The p_{\perp} -projected DOS on bulk and edge atoms for the nanoribbon with and without C_7 chain are reported in fig. 5.40 along with the p_{\parallel} and p_{\perp} projections on chain atoms.

The π_{\parallel} chain states remain rather localized in energy, indicating that they do not strongly couple with the ribbon, except the *HOMO*, lying in the region [-0.2, 1.5] eV, which partially depleted ($\sim 0.6 |e|$ are transferred to the σ states), suggesting that it is involved in the formation of the chain-electrode bond. As opposite π_{\perp} chain states are largely broadened in energy as a consequence of the strong coupling, except the *HOMO*, which turns out to be in the region characterized by a small number of edge and bulk states.

The binding of the chain does not induce deep modifications in the bulk and edge projected DOS, except for a rigid shift by ~ 0.2 eV at lower energies. By integrating the DOS, we found that the binding of the chain causes a small reduction of the charge transfer both from the π_{\perp} to the σ states of bulk atoms (~ 0.070 vs $\sim 0.074 |e|/\text{atom}$ for the ribbon without chain) and from bulk to edge π_{\perp} states (~ 0.012 vs $\sim 0.015 |e|/\text{atom}$), hence the chain stabilizes the π electron clouds of the electrodes. No charge transfer has been found between the π_{\perp} states of the chain and the ribbon. Moreover we noticed that the chain states induce minor modifications in the edge states with respect to the zigzag case, indicating that the chain more strongly hybridizes with the zigzag edge than with the armchair one.

A similar behavior has been observed for C_7 3R, mainly differentiating only for the reduced broadening of π_{\perp} chain states, due to the weak chain-electrode coupling, and for a negligible charge transfer from the π_{\parallel} to the σ states of the chain.

The DOS analysis for C_7 5R is reported in fig. 5.41. It is evident that the further increasing of the chain-electrode bond length and the consequent stretching of the chain remarkably reduce the broadening of the π_{\perp} chain states, with respect to C_7 and C_7 3R. Moreover, as a consequence of the weak coupling, the binding of the chain does not induce any modification in the charge transfer in the bulk region and from the bulk to the edge. On the other hand, the π_{\parallel} chain states resemble the behavior of C_7 with $\sim 0.7 |e|$ transferred to σ states causing the *HOMO* to partially deplete and significantly broaden in energy.

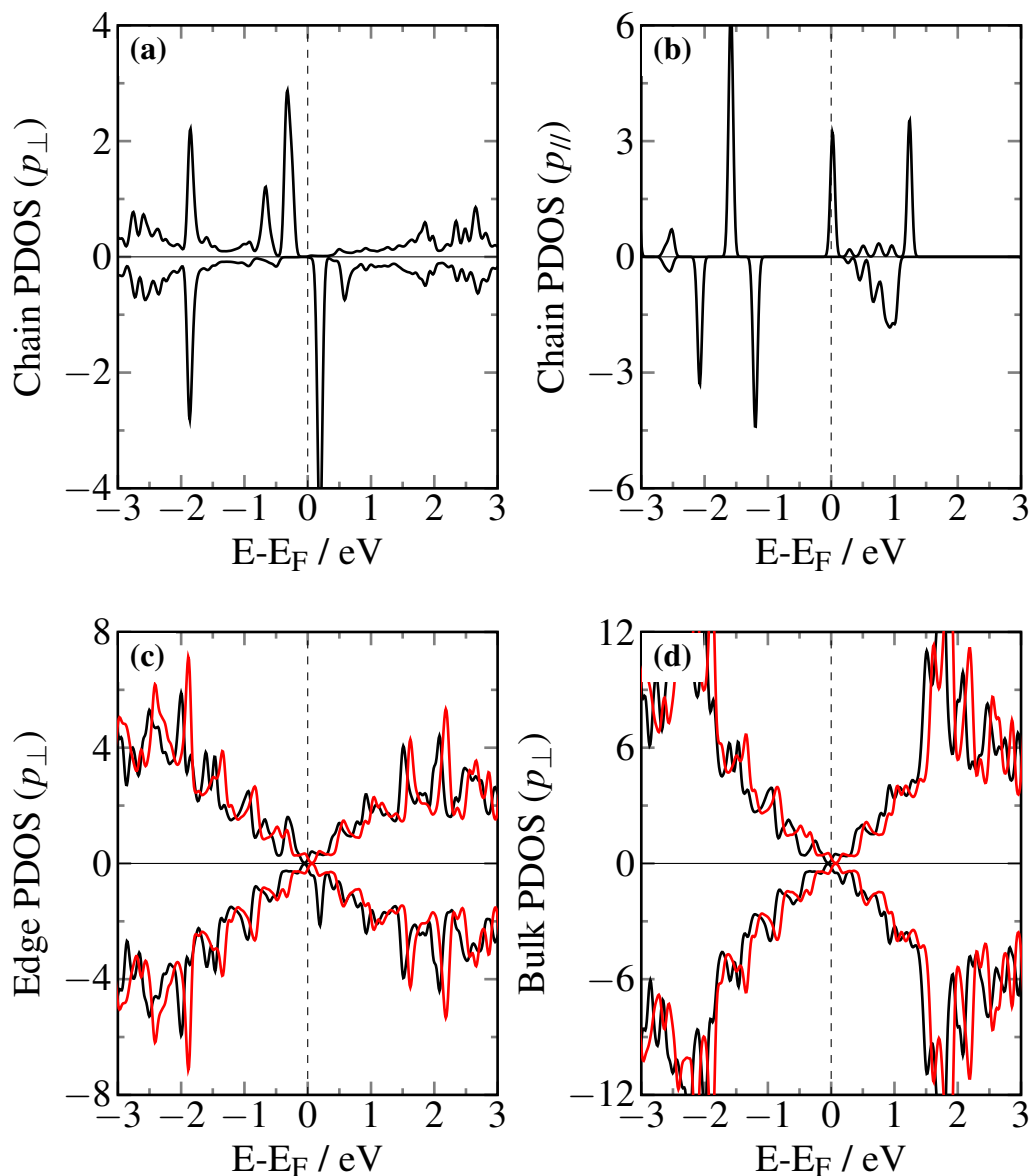


FIGURE 5.40: Density of states for the armchair nanoribbon connected through a C_7 chain (black) and without chain (red). Results have been portrayed for spin majority (upper curves) and spin minority (lower curves) components. (a) DOS projection onto the p_{\perp} orbitals of the chain. (b) DOS projection onto the p_{\parallel} orbitals of the chain. (c) p_{\perp} projected DOS for edge atoms. (d) p_{\perp} projected DOS for bulk atoms.

Finally we computed the transmission spectra for C_7 and C_8 chains, for all junction configurations. The results are reported in fig. 5.42 and 5.43, respectively. The spectrum of C_7 , unlike the zigzag case, does not show a low-conductive window in the Fermi level region, although at the Fermi level the transmission tends to zero, reflecting the shape of the DOS of the (semi-infinite) graphene electrodes. However this region turns out to be weakly conductive since the *HOMO* is essentially decoupled from bulk states, giving a very small contribution to the transmission probabilities, which result to be

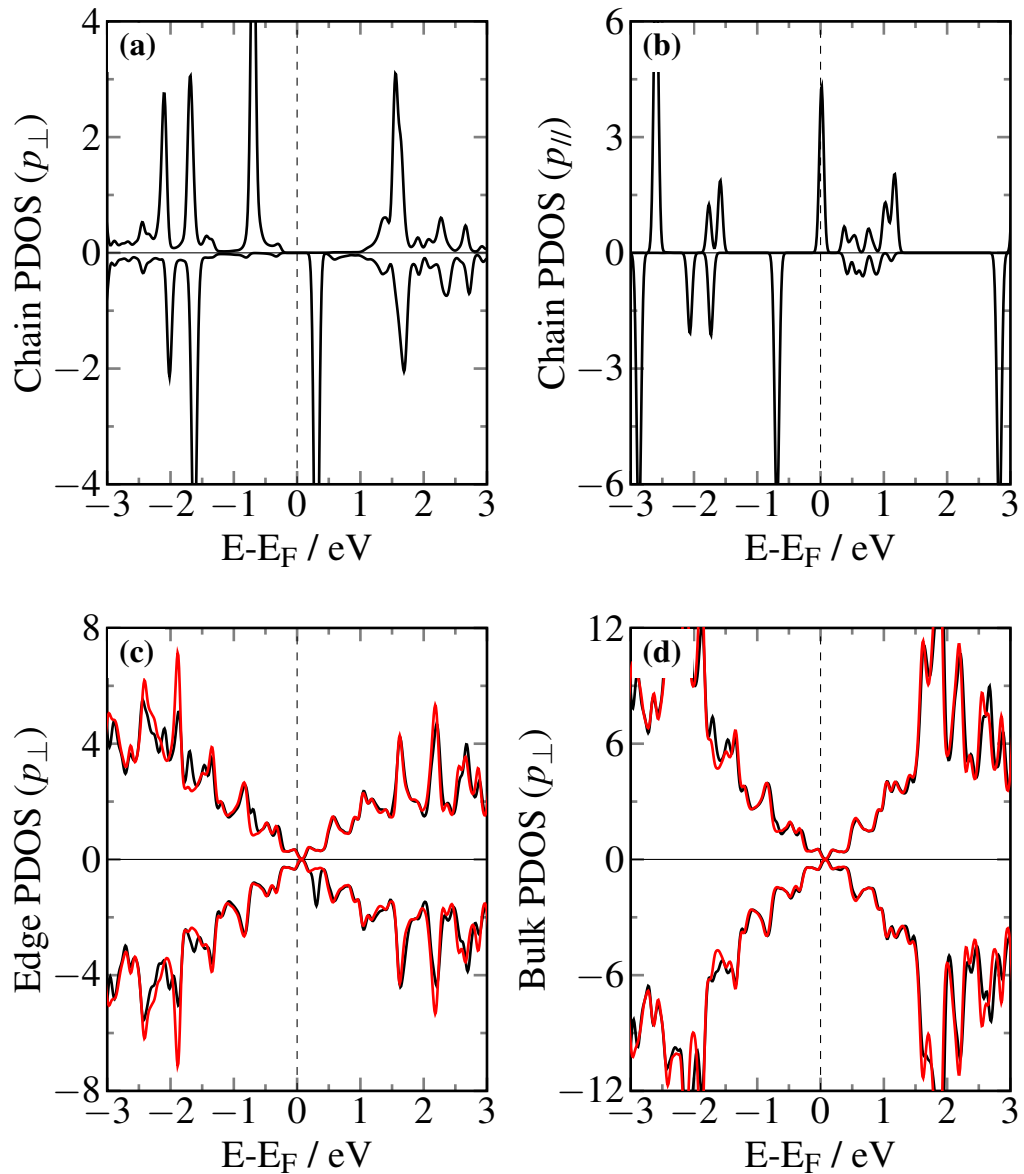
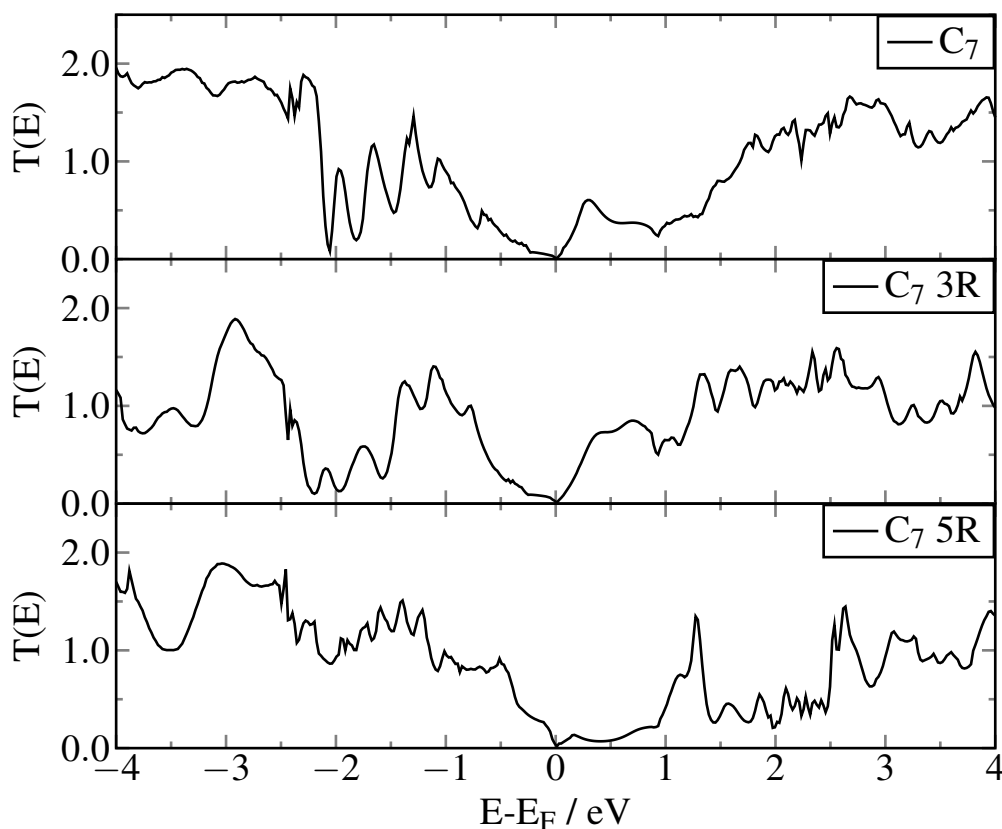


FIGURE 5.41: Density of states for the armchair nanoribbon connected through a C_7 5R chain (black) and without chain (red). Results have been portrayed for spin majority (upper curves) and spin minority (lower curves) components. (a) DOS projection onto the p_{\perp} orbitals of the chain. (b) DOS projection onto the p_{\parallel} orbitals of the chain. (c) p_{\perp} projected DOS for edge atoms. (d) p_{\perp} projected DOS for bulk atoms.

mainly determined by the tails of the $HOMO_{-1}$ and $LUMO$ states. Moreover, unlike zigzag-bound chain, the maximum transmission probabilities turns out to be considerably lower than the maximum allowed, and only below -2 eV the transmission approaches such value. We suggest that this is related to the weaker coupling of the chain with the armchair edge with respect to the zigzag edge.

The transmission spectrum of C_7 3R features only minor differences with respect to C_7 , reflecting the similar BLA of the two structures. Specifically the weaker coupling

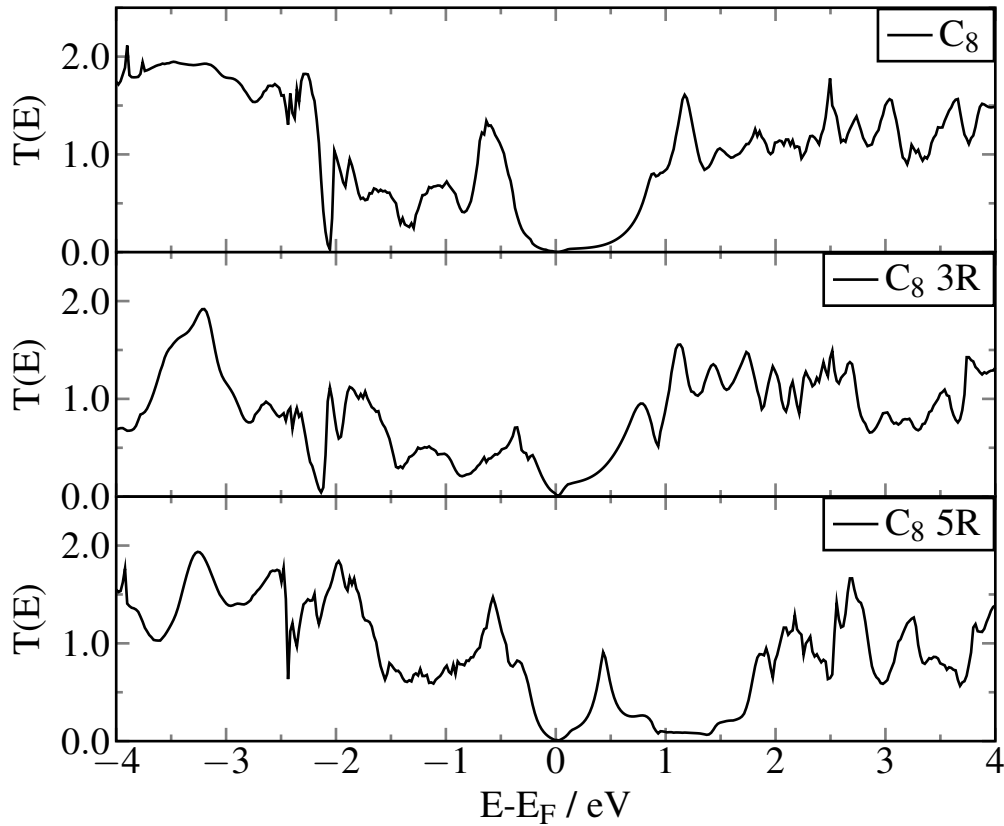
FIGURE 5.42: Transmission spectra of C_7 , C_7 3R and C_7 5R

with the electrode causes the chain states to be less broadened and to slightly approach the Fermi level, determining a small increasing of the transmission probabilities in the region $[-1.0, 1.0]$ eV and a sizable reduction below -2 eV.

For C_7 5R, the long chain-electrode bond length leads to a general reduction of the transmission probabilities, particularly evident for the empty states, determining a region just above the Fermi level characterized by very low transmission probabilities.

C_8 features transport properties somehow similar to C_7 (see fig. 5.43), except for a strong reduction of the transmission probabilities close to the Fermi level as a consequence of the gap in the π_{\perp} chain states, due to the polyynic structure of the chain. Below the Fermi level, the transmission spectrum features a moderately conductive region dominated by the $HOMO$ state (from -2 to 0 eV) followed by an highly conductive one, dominated by $HOMO_{-1}$ (below -2 eV) in correspondence of the region with an increasing contribution of bulk states in the DOS. Above the Fermi level, the $LUMO$ and the $LUMO_{+1}$ states are considerably broadened in energy and partially overlap, giving rise to unresolved resonances in the transmission spectrum.

In the C_8 3R case the $HOMO - LUMO$ gap is reduced with respect to the previous case, probably as a consequence of the more radicalic character of the chain. It follows an

FIGURE 5.43: Transmission spectra of C_8 , C_8 3R and C_8 5R

increasing of the transmission probabilities close to the Fermi level, although the significant reduction of the chain-electrode coupling causes an overall diminution of the transmission elsewhere. Specifically the *HOMO* states gives rise to the non-resolved resonance at ~ -0.45 eV, while the *LUMO* holds the conduction process from the Fermi level to ~ 3.5 eV.

Similar is the behavior of C_8 5R, differentiating mainly for a general shift downwards in energy of the chain states, causing the *LUMO* to lie just above the Fermi level (~ 0.5 eV) causing a significant reduction of the transmission in the region $[0.0, 1.5]$ eV. On the other hand the *HOMO* state, lying at ~ -0.75 eV turn out to be more hybridized with bulk states with respect to 3R case, determining an increasing in the magnitude of the corresponding resonance.

